The Impact of Vertical Wind Shear on Hail Growth in Simulated Supercells

Eli J. Dennis and Matthew R. Kumjian

Department of Meteorology and Atmospheric Science, The Pennsylvania State University, University Park, Pennsylvania

ABSTRACT

Severe hailstorms produce over \$1 billion in insured losses annually in the United States, yet details of a given storm's hail threat (e.g., maximum hailstone size and total hailfall) remain challenging to forecast. Previous research suggests that, in addition to maximum updraft speed, the storm-relative airflow could be equally important for hail formation and growth. This study is a first step toward determining how changes in environmental wind shear and subsequent changes in simulated supercell storm structure affect hail growth. Using Cloud Model 1 (CM1) with 500-m horizontal and 250-m vertical grid spacing, 20 idealized simulations are performed in which the thermodynamic profile remains fixed but the environmental hodograph is systematically altered. Hail growth is quantified using the hail mass mixing ratio from composites of storms over the last hour of simulation time. Hailstone growth "pseudotrajectories" are computed from these storm composites to determine favorable embryo source regions.

Results indicate that increased deep-layer east–west shear elongates the storm's updraft in that direction, providing 1) increased volumes over which microphysically relevant hail processes can act, 2) increased hailstone residence times within the updraft, and 3) a larger potential embryo source region; together, these lead to increased hail mass. Increased low-level north–south shear, which results in hodographs with increased 0–3-km storm-relative helicity, also elongates the updraft in the north–south direction. However, hail mass is reduced owing to a separation of favorable embryo source regions (which shift southward) and available hydrometeors to serve as embryos (which shift northward).

1. Introduction and motivation

The large number of hailstorms that occur each year in the United States make these severe convective storms collectively one of the costliest hazards in terms of insured losses to homes, businesses, automobiles, aircraft, and agriculture. Annual insured losses in the United States from hailstorms exceed \$1 billion (Munich Re 2013). Moreover, individual hailstorms can produce hundreds of millions of dollars to over \$1 billion in damage (e.g., Picca and Ryzhkov 2012), including the San Antonio 12 April 2016 storm, which is estimated to have produced \$1.36 billion in damage (NWS–San Antonio 2016). Other parts of the world are affected as well. Recently, a series of hailstorms in Germany unexpectedly led to losses in excess of EUR 3 billion (Munich Re 2014). Thus, understanding processes contributing to hail formation, hail growth, and the environmental controls over hail production are important

for anticipating hail threats and potentially mitigating the risk (e.g., moving automobiles and aircraft to cover).

A large thrust in hail-related research occurred during the 1970s as a part of the National Hail Research Experiment (NHRE), a large multidisciplinary project with an ultimate aim of weather modification and hail suppression (e.g., Foote and Knight 1979). Regarding hail suppression, the results showed little hope: Knight et al. (1979, p. 1630) summarize the project's findings by stating "no influence of seeding on hailfall has been detected." Funding and interest in hail suppression research faded after this project (C. Knight 2014, personal communication). However, several of the well-sampled storms during NHRE and other campaigns were the subject of further research exploring the mechanisms of hail formation and growth in convective storms. Many found that the storm's airflow patterns were just as important for hail production (if not more important) than its maximum updraft speed. Several of these studies have shown that hail growth can occur from numerous initial conditions, but the favorable initial region for hail embryos is restricted (e.g., Foote 1984). Growth of embryos into large hailstones depends on the trajectories

Corresponding author e-mail: Dr. Matthew Kumjian, kumjian@psu.edu

they take through the storm's updraft. For supercells in particular, three main embryo trajectories have been proposed (e.g., Browning and Foote 1976, their Fig. 19; Conway and Zrnić 1993): 1) embryos enter a region of strong updraft and are ejected through the forward anvil before significant growth can occur; 2) embryos enter the less-intense western edge of the updraft, grow at moderate rates in ascent, and cycle into the re-flectivity overhang (known as the "embryo curtain"); and 3) embryos from 2) fall cyclonically around the updraft and recycle at the bottom of the embryo curtain into a region of the updraft where a balance is achieved between updraft velocity and hailstone fall velocity. In this crucial suspended state, hailstones can experience prolonged exposure to regions where optimal growth conditions may exist.

Numerous studies point out that this balance is a key condition for optimum hail growth (e.g., Browning 1964; Foote 1984; Heymsfield 1983; Nelson 1983; Miller and Fankhauser 1983; Musil et al. 1986; Miller et al. 1990; Conway and Zrnić 1993; Kennedy and Detwiler 2003; Grant and van den Heever 2014, hereafter GvdH14). If the updraft is too strong, small particles will be ejected out of the top of the growth region too quickly to ex-perience significant growth; if it is too weak, embryos simply sediment out before substantial growth can occur (e.g., Browning and Foote 1976; Nelson 1983; Foote 1984; Musil et al. 1986; Rasmussen and Heymsfield 1987). Though the maximum updraft intensity does place an upper limit on hailstone size, high-speed up-drafts are insufficient to ensure that large stones are grown; stones must also reside in the updraft for enough time, and this is largely governed by the horizontal path growing hailstones take through the updraft (Nelson 1983; Miller et al. 1990). In part, this depends on the width of the updraft, with broader updrafts favored for enhanced hail growth (e.g., Nelson 1983; Foote 1984).

Foote (1984) shows embryos that have grown by some mechanism to millimeter-sized diameters before entering the updraft are most likely to achieve the required bal-ance between fall speed and updraft speed. This balance must occur in a region with sufficient supercooled liquid water (cloud droplets and raindrops) and an appropriate temperature for efficient growth. For large-hail growth, the hailstones/embryos must be balanced such that they experience prolonged exposure to the moisture-rich up-draft at temperatures between $-10°$ and $-25°C$ (e.g., Nelson 1983; Ziegler et al. 1983; Foote 1984; Miller et al. 1988). However, competition among embryos for super-cooled liquid water has also been cited as a limiting factor for hail growth (e.g., Heymsfield 1983).

To summarize, optimal hail growth is dependent on five key characteristics: 1) appropriate updraft strength and breadth to facilitate the suspension of hailstones/ embryos, 2) sufficient amounts of supercooled liquid water, 3) temperatures conducive to hail growth, 4) the size and number of embryos such that the particles are balanced in the updraft and competition does not de-plete the total water content, and 5) trajectories that take these embryos through the optimal growth envi-ronments. Regarding the latter, Nelson (1987) argues that storm airflow patterns are "critically important" for controlling severe hail events, a conclusion echoed by numerous other studies cited above. However, none of these studies systematically investigated how environ-mental factors alter supercell airflow patterns and thus hail production.

The structure and intensity of supercell storms has been explored extensively in the last half century. Nu-merical simulations examining the effects of varying unidirectional vertical wind shear and buoyancy (CAPE) on idealized convective storms were carried out by Weisman and Klemp (1982). They found a spectrum of storm behaviors similar to observed storms, including short-lived single-cell storms, multicell storms, and su-percells. For fixed CAPE, they found increasing shear decreases maximum updraft intensity and increases the updraft tilt. A follow-up study (Weisman and Klemp 1984) tested the influence of directionally varying wind shear on simulated convective storms. Their results were qualitatively similar to their previous work but added insights into how clockwise-turning hodographs favor cyclonically rotating supercells. Varying only midlevel shear, Brooks et al. (1994) found differences in the de-velopment, maintenance, and intensity of *low-level* mesocyclones, identifying the strength of the midlevel storm-relative flow as being critical for the simulated supercell precipitation structure. Weisman and Rotunno (2000) simulated supercells in environments with straight through circular hodographs to clarify mecha-nisms by which convective storms acquire rotation and propagate across the environmental vertical shear. McCaul and Weisman (2001) found that stratification of buoyancy and shear and shapes of their profiles cause substantial impacts on updraft intensity, cold pool in-tensity, and midlevel and surface vorticity.

Though these studies have greatly advanced our un-derstanding of supercell storm structure and dynamics and how these vary with environmental parameters, less attention has been paid to how these variations alter microphysics and, specifically, hail formation and growth. Van den Heever and Cotton (2004) analyzed the resulting changes to storm structure and evolution by modifying hail size distribution parameters in a single-moment microphysics scheme. However, these changes to the hail size distribution were made a priori,

without explanation of how these may arise; thus, the authors call for a better understanding of how environmental factors (including aerosol concentrations, the presence of dry layers, and vertical wind shear) influence the hail size distribution.

More recently, GvdH14 analyzed the impact of varying midlevel relative humidity on resulting simulated supercell structure and hail production. They found that changes in storm-relative winds led to different hail growth mechanisms in "low precipitation" supercells versus "classic" supercells. Classic supercells had the largest riming rates on the western side of the updraft, whereas low-precipitation supercells had the largest riming rates on the north and northeast sides of the updraft. Whereas the observational study of Rasmussen and Straka (1998) suggested anvil-level storm-relative winds could be a factor in determining supercell mode (with low-precipitation supercells favored in environments with larger anvil-level storm-relative winds), the differences in GvdH14 arose from changes in storm motion and storm-scale-generated flow in each simulation, in which midlevel relative humidity was changed but environmental wind profiles were fixed.

In contrast, this study aims to investigate the role of environmental wind profiles on supercell structure and subsequent hail growth. The next section describes the methods used and the numerical simulations performed. Results are presented in section 3. Section 4 provides a discussion of the results and outlines the main conclusions of this study.

2. Methods

To investigate the impact of environmental shear on hail growth in idealized supercell storms, a series of idealized simulations is performed. Cloud Model 1 (CM1; Bryan and Fritsch 2002), version 17, is used for these simulations, with a 240 × 240 × 80 grid using 500-m horizontal grid lengths and 250-m vertical grid lengths. In each simulation, the thermodynamic environment is fixed (CAPE = 2200 J kg^{-1}), using the idealized supercell sounding from Weisman and Rotunno (2000). The simulations were run for 2 h using a 1.5-s time step, with output files written every 5 min. Lateral boundaries are gravity wave radiating, similar to Klemp and Lilly (1978) and Klemp and Wilhelmson (1978), but with a modification to prevent mass leakage from the domain (G. Bryan 2016, personal communication). The lower boundary is free slip with no fluxes considered. The domain is translated with storm motion to keep the storm centered in the domain. Storm motion was determined by following the midlevel updraft core in a simulation with a stationary domain. The average motion over the simulation period was applied. This was done for each of the simulations herein, resulting in different translation speeds for each storm. Though admittedly redundant, this allowed for more accurate storm motion estimates than those based on the hodograph alone. This observed storm motion was used to compute storm-relative helicity from the prescribed hodographs.

A Rayleigh dampening layer is applied in the stratosphere, in the upper 5 km of the domain. Storms are initiated with a warm (1-K potential temperature perturbation) bubble. The two-moment Morrison microphysics scheme (Morrison et al. 2005, 2009) is used, with the rimed ice category set to the high-density option ("hail"). In the standard version of the two-moment Morrison scheme, cloud droplet number concentration is held constant at 250 cm^{-3}. Assuming a fixed cloud liquid mass mixing ratio, changes in this droplet number concentration would alter droplet sizes. Although this effect can be important for hail production and other microphysical process rates (e.g., Lebo 2014; Kalina et al. 2014; Loftus and Cotton 2014), this and other aerosol effects are not accounted for in the present study.

The idealized "quarter circle" hodograph of Weisman and Rotunno (2000) is the base wind profile for this study. The east–west (u) and north–south (v) wind components are given as follows:

$$u = u_{\max 1} - u_{\max 1} \cos(\theta) \quad \text{for} \quad z \leq h_1, \tag{1}$$

$$u = u_{\max 1} + (z - h_1)\frac{(u_{\max 2} - u_{\max 1})}{h_2 - h_1} \quad \text{for} \quad h_1 < z \leq h_2, \tag{2}$$

$$u = u_{\max 2} \quad \text{for} \quad z > h_2, \tag{3}$$

$$v = v_{\max} \sin(\theta) \quad \text{for} \quad z \leq h_1, \tag{4}$$

$$v = v_{\max} \quad \text{for} \quad z > h_1, \tag{5}$$

where

$$\theta = \frac{\pi z}{2h_1}. \tag{6}$$

In the control run, $u_{\max 1} = 7.0\,\text{m s}^{-1}$, $u_{\max 2} = 31\,\text{m s}^{-1}$, $v_{\max} = 7\,\text{m s}^{-1}$, $h_1 = 2\,\text{km}$, and $h_2 = 6\,\text{km}$. (These are the parameter settings in the standard CM1 package quarter-circle hodograph supercell case.) The main parameters altered in this study are $u_{\max 2}$, which changes the hodograph's east–west length, and $v_{\max}$, which changes its north–south length. Table 1 lists the simulation names, along with the total 0–6-km hodograph length and 0–3-km storm-relative helicity computed following Markowski and Richardson (2010) using the simulated storms' motions. These values were chosen

TABLE 1. Simulations performed for this study. Naming convention includes the value of the u_{max2} and v_{max} parameters. If no v_{max} value is listed, the default value of $7\,m\,s^{-1}$ is used. Also listed are the total (0–6 km) hodograph length and 0–3-km storm-relative helicity.

Storm	Hodograph length ($m\,s^{-1}$)	Storm-relative helicity ($m^2\,s^{-2}$)
umax25	29	90
umax25vmax10	32	122
umax25vmax13	35	156
umax25vmax16	38	194
Control (umax31)	35	113
umax31vmax10	38	152
umax31vmax13	41	197
umax31vmax16	44	233
umax36	40	135
umax36vmax10	43	177
umax36vmax13	46	225
umax36vmax16	49	266
umax41	45	156
umax41vmax10	48	199
umax41vmax13	51	225
umax41vmax16	54	266
umax50	54	200
umax50vmax10	57	279
umax50vmax13	60	342
umax50vmax16	63	410

subjectively to cover the range of hodograph lengths (proxy for 0–6-km shear) observed for supercells (e.g., Marwitz 1972; Brooks et al. 1994), but with some variability of the low-level storm-relative helicity.

Of relevance for storm structure and microphysics is the *storm-relative* flow. Although vertical wind shear is Galilean invariant, how it is partitioned into u and v components may change depending on storm motion. For typical supercell environments, most turning of the hodograph occurs in the lowest few kilometers, followed by roughly unidirectional shear aloft, which tends to be zonal on average in North America (e.g., Maddox 1976; Weisman and Rotunno 2000; Markowski et al. 2003; Markowski and Richardson 2010). The analytic quarter-circle hodograph used herein has deep-layer unidirectional shear in the east–west direction (u component), whereas the hodograph turning at low levels is associated with north–south (v component) shear. Clearly, other cases (e.g., in a northwest flow regime) would not conform well to such a u and v partitioning. However, for simplicity we adopt the u- and v-component terminology for this study.

A detailed understanding of how hail sizes change with environmental factors requires the use of sophisticated bin microphysical models (e.g., Lebo et al. 2012). This is because bulk schemes do not adequately treat processes like size sorting that can affect the tails of the

particle size distributions (e.g., Milbrandt and Yau 2005a; Wacker and Seifert 2001; Milbrandt and McTaggart-Cowan 2010; Dawson et al. 2010; Kumjian and Ryzhkov 2012). Though some three-moment schemes have been developed and/or used to mitigate many of these concerns (e.g., Milbrandt and Yau 2005b; Kumjian and Ryzhkov 2012; Dawson et al. 2014; Loftus et al. 2014), these are not widely available in CM1 or WRF and thus are not used in the present study. As such, we focus on hail production in terms of the total mass mixing ratio and refrain from much discussion of hailstone sizes. Future work focusing specifically on hail sizes should use more detailed bin microphysical models that most realistically treat the evolution of the particle size spectrum.

3. Analysis and results

The simulation results are presented in this section and are divided into subsets to focus on the impacts of changing individual parts of the hodograph at a time.

a. The u-component (deep layer) shear

The first subset of simulations includes those for which only the u_{max2} parameter (here u_{max}) is varied, leading to hodographs with variations in only the east–west component of the shear. For typical U.S. supercells, this is analogous to increasing the deep-layer (0–6-km) shear. Recall that the control case has $u_{max} = 31\,m\,s^{-1}$; here, we additionally set u_{max} to 25, 36, 41, and $50\,m\,s^{-1}$. The hodographs for each of these simulations are shown in Fig. 1, and properties of these hodographs can be found in Table 1.

Modifying the environmental shear is expected to have an impact on the subsequent storm structure and evolution. To assess any changes in updraft speed, time series of 1-min maximum vertical velocity for each of the simulations are shown in Fig. 2. From the figure, it is evident that maximum updraft speeds were slightly different among the different simulations. When averaged over the last 40 min, the highest and lowest average maximum updraft speed did not differ by more than $7\,m\,s^{-1}$. There is, however, an inverse relationship between the average maximum updraft strength and u-component shear: the highest-shear case (umax50) has the lowest average maximum updraft strength over the last 40 min of the simulation, whereas the lowest-shear case (umax25) has the strongest updraft. Thus, stronger east–west (u component) shear leads to slower-developing storms and slightly reduced w_{max}, consistent with the findings of Weisman and Klemp (1982). The reduced w_{max} for a given amount of CAPE may be related to the effects of
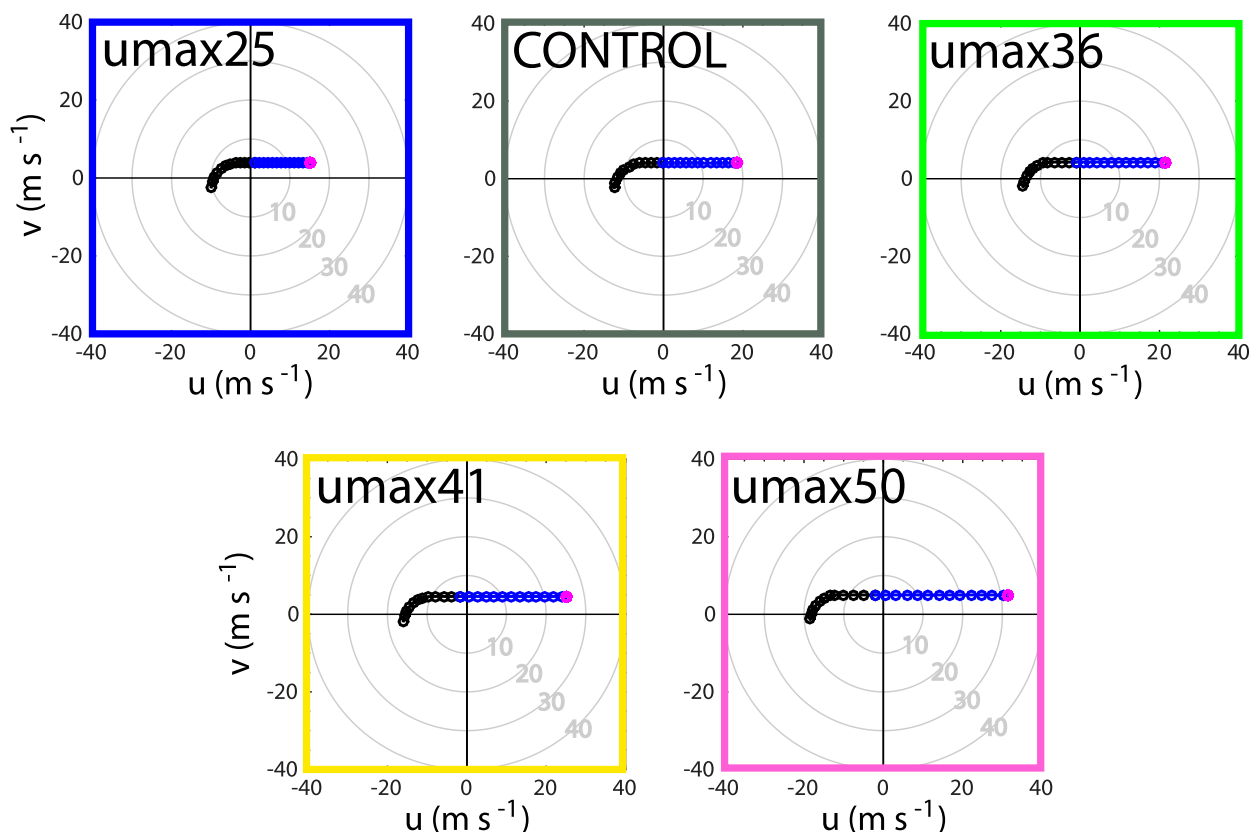
FIG. 1. Storm-relative hodographs for the subset of supercell simulations in which only the deep-layer east–west (u) component of the shear is varied. The naming convention for each storm is indicated in the upper left of each panel; it refers to the u_{max2} value (m s^{-1}) from (2) and (3) (see Table 1). The control run is the standard CM1 supercell case and is equivalent to umax31. Each of these storms has $v_{\mathrm{max}} = 7$ m s^{-1}. Winds in the lowest 3 km are shown in black, 3–6-km winds in blue, and >6-km winds in magenta. Color frames around each panel are consistent with subsequent figures.

the downward-directed perturbation pressure gradient force arising from buoyancy gradients atop updrafts. The magnitude of this perturbation pressure gradient force has been shown to increase for broader (e.g., Markowski and Richardson 2010; Morrison 2016a,b) and tilted (Parker 2010) updrafts. As shown below, updrafts in the higher-shear cases indeed are broader.
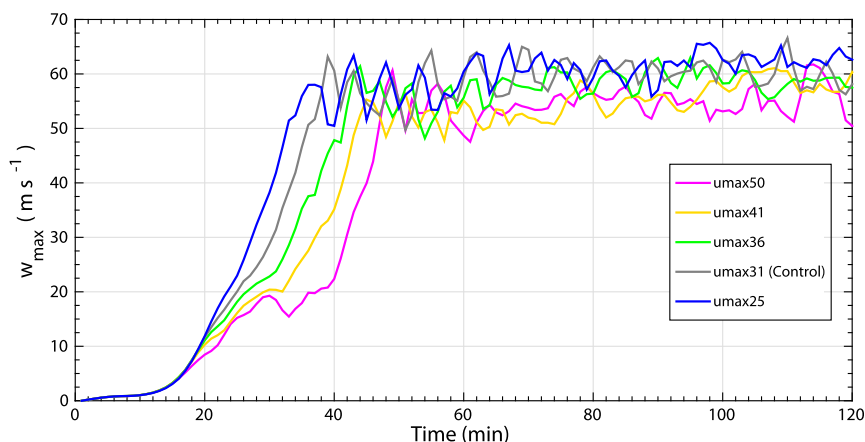
FIG. 2. Time series of the maximum vertical velocity w_{max} (m s^{-1}) for the five u_{max} storms.
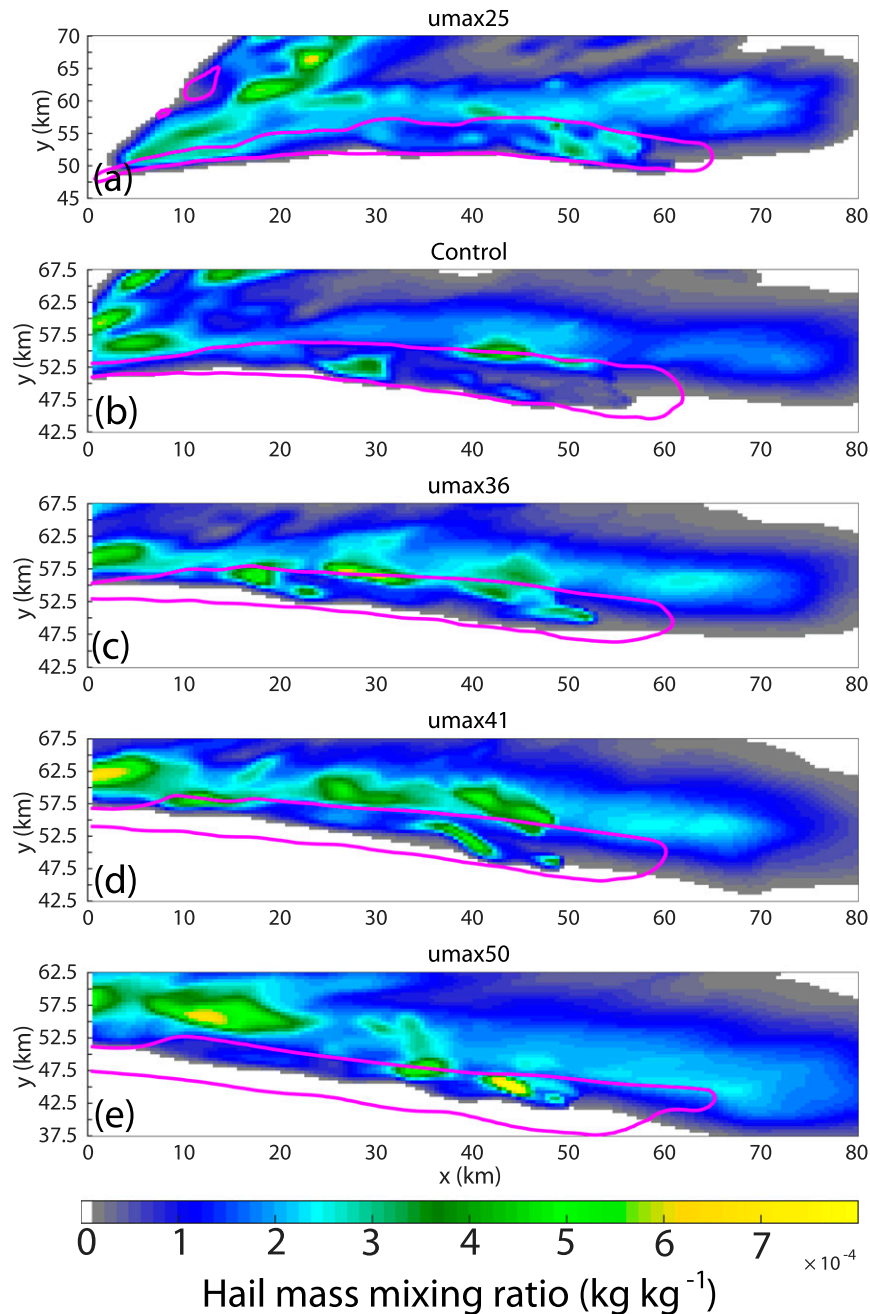
FIG. 3. Time-integrated maximum hail mass mixing ratio (shaded according to scale; $kg\,kg^{-1}$) at the lowest model grid level with a moving domain throughout the 2-h storm simulation for each of the u_{max} storms. Overlaid is the trace of the 5-km-AGL updraft $30\,m\,s^{-1}$ contour (magenta).

Simulated hail swaths of maximum hail mass mixing ratio at the lowest model grid level are shown in Fig. 3, overlaid with the $30\,m\,s^{-1}$ 5-km-AGL updraft contour (magenta line). Each reveals an elongated, ~10-km-wide swath of lower values ($<2 \times 10^{-1}\,kg\,kg^{-1}$), within which are embedded localized maxima that tend to favor

the southern edge of the swath. However, differences exist between the simulations. For example, the high-shear cases (umax41 and umax50) appear to have larger values in these embedded maxima; peak values approach $1.0 \times 10^{-3}\,kg\,kg^{-1}$ in the umax50 case. Additionally, higher-shear cases feature less hail mass
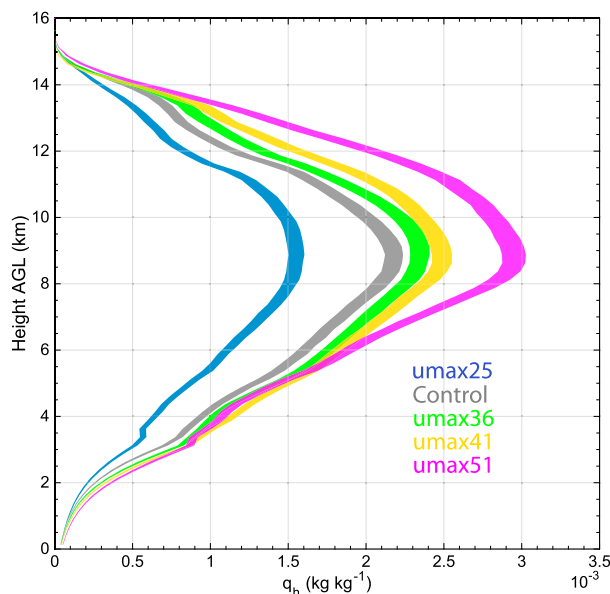
FIG. 4. Vertical profiles of the 95% confidence intervals about the average hail mass mixing ratio q_h for each storm, computed from the composites.

TABLE 2. Microphysical processes in the Morrison two-moment scheme relevant to hail formation and growth. Processes are combined into categories discussed in this study.

Category	Process
Freeze conversion	Immersion freezing of raindrops to form hail
	Conversion of rain to hail due to collisions between rain and cloud ice (contact freezing)
	Conversion of cloud ice to hail due to collisions between rain and cloud ice (contact freezing)
Rime conversion	Conversion to hail via riming (snow collecting raindrops)
	Conversion to hail via riming (snow collecting cloud droplets)
	Conversion to hail via riming (raindrops collecting snow)
Rime growth	Growth of hail by collection of raindrops
	Growth of hail by collection of cloud droplets
Depositional growth	Growth of hail by vapor deposition

directly beneath the midlevel updraft core. Given the spatiotemporal variability of hailfall characteristics in these storms, robust comparisons of the storm's structure are desired. To do so, we construct composites for each storm to determine the average structural features during their mature phase.

Composites of each simulated storm are produced following methods similar to those used in GvdH14. First, the right-moving supercell's midlevel (6.125 km AGL) updraft maximum is found for each output time during the last hour of simulation. The data are recentered on this midlevel updraft maximum, and the domain is constricted to ±25 km in the x and y directions from this center. Then, each field on the 50 km × 50 km recentered grid from each time is averaged.

Figure 4 shows vertical profiles of the average hail mass mixing ratio q_h computed from the composites for each of the u-component shear subset of cases. To assess the statistical significance of differences in the average q_h at a given altitude, we used a bias-corrected-and-accelerated bootstrapping technique (e.g., Efron and Tibshirani 1993) with 1000 resamples to estimate the 95% confidence intervals about the average q_h profiles. If the confidence intervals of different simulations are separated, one may infer that there are statistically significant differences in the composited q_h fields between these simulations. The separation of the 95% confidence interval bands at most altitudes demonstrates that increasing the u-component shear results in statistically significant increases in q_h.

So, changing the u-component (deep layer) shear via the u_{max} parameter has a statistically significant impact on hail production: increasing u-wind shear leads to larger average hail mass mixing ratios, particularly aloft. Similarly, number mixing ratio magnitudes increase with increasing u shear, except for the umax50 case below ~11.4 km (not shown). At lower levels, reductions in hail mass occur at different rates that cannot be attributable to thermodynamics, given the fixed profiles used. Rather, investigations of mean-mass diameter (not shown) suggest size sorting effects play a large role in modulating melting rates. These issues likely stem from excessive size sorting in two-moment schemes and contribute to the inability of two-moment schemes to produce much hail at the surface (e.g., Loftus et al. 2014). Indeed, excessive size sorting effects are evident as large mean-mass hail diameters at the surface along the inflow side of the forward flank, as in other studies (e.g., Kumjian and Ryzhkov 2008; Dawson et al. 2014; Kumjian et al. 2015).

To determine the underlying reason for the differences in hail production aloft, we first investigate whether certain microphysical processes are acting at higher rates in the high-shear cases. In the Morrison two-moment microphysics scheme, there are several microphysical processes relevant for hail formation and growth (Table 2). These can be broadly categorized into conversion processes, in which the particles are converted from some other hydrometeor category to hail, or growth processes, in which mass is added to existing hail. After consulting with the parameterization scheme's
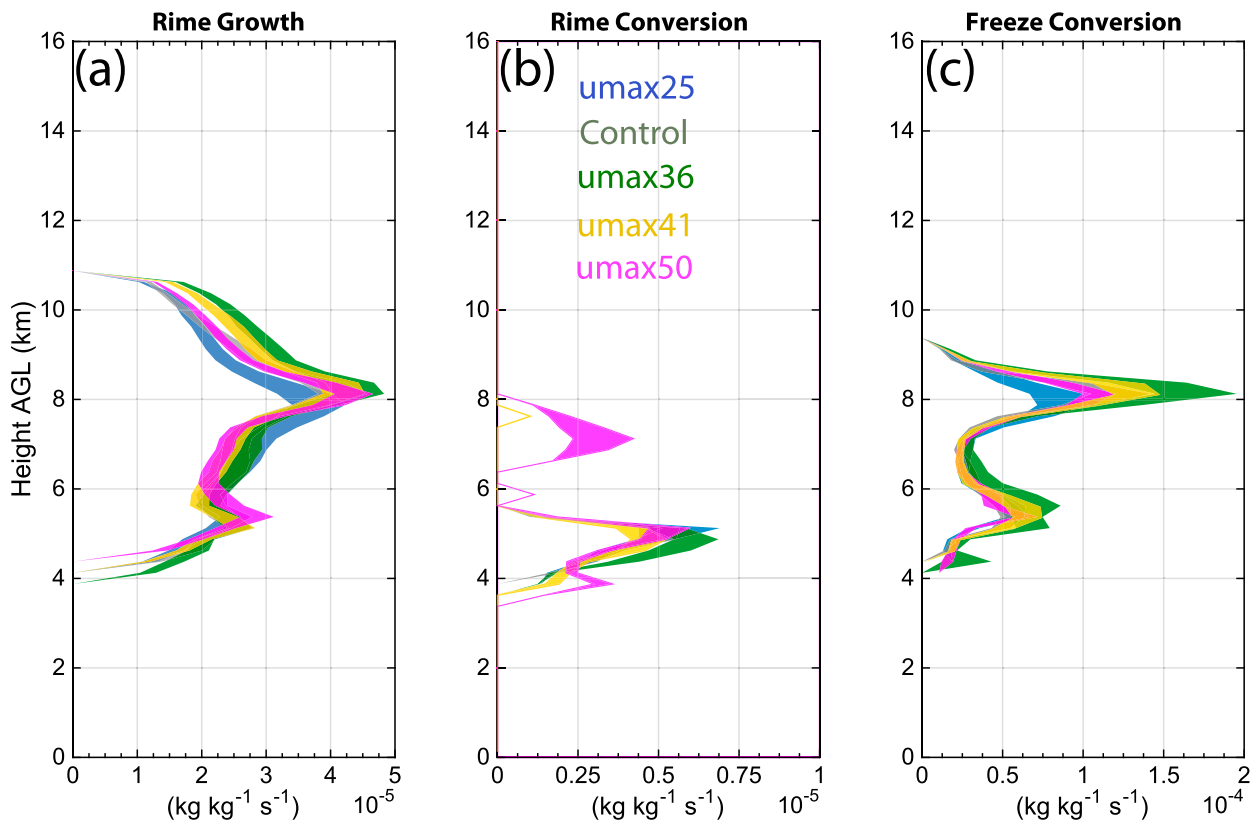
FIG. 5. Vertical profiles of the 95% confidence intervals about the conditionally averaged microphysical process rates for each u_{max} subset storm, computed from the composites: (a) rime growth, (b) rime conversion, and (c) freeze conversion. Note the different ranges of values on the abscissa.

architect (H. Morrison 2014, personal communication), we have combined these process rates into four broad categories: conversion to hail by freezing, which includes immersion freezing of raindrops and contact freezing of raindrops resulting from collisions with cloud ice; conversion to hail by riming, which includes riming of snow by raindrops and cloud droplets; growth of hail by riming, which includes collection of raindrops and cloud droplets; and vapor depositional growth of hail. For brevity, hereinafter these are referred to as freeze conversion, rime conversion, rime growth, and deposition growth, respectively (Table 2). In the Morrison two-moment scheme, only a portion of the mass acquired from riming is converted to hail, following Reisner et al. (1998). Additionally, mass mixing ratios of the species involved with riming must exceed $0.1 \, g \, kg^{-1}$ for conversion to be active (Morrison and Grabowski 2008). Deposition growth is not included in the subsequent analyses because its rate was at least an order of magnitude less than the other categories in our simulations.

For each of the simulations, vertical profiles of the processes rates are conditionally averaged for the composites over the last hour of the simulations, computed

along with their 95% confidence interval about that mean at each height level. Grid boxes were only included in the averages if the process rates exceeded $1 \times 10^{-5} \, kg \, kg^{-1} \, s^{-1}$ for rime growth and freeze conversion, and $1 \times 10^{-6} \, kg \, kg^{-1} \, s^{-1}$ for rime conversion. These thresholds were tested over a range of orders of magnitudes, and the qualitative results were not affected. The statistics were again estimated using the bootstrapping technique (e.g., Efron and Tibshirani 1993) with 1000 resamples. The 95% confidence intervals about the average vertical profiles of the process rates are shown in Fig. 5. Though differences between the various simulations do exist, many of the confidence intervals indeed overlap. Further, there is no clear relationship between the magnitude of the process rates and hail production. For example, much of the domain below 8 km AGL reveals lower rime growth rates in the umax50 storm (Fig. 5a), which had the largest surface hail mass mixing ratio. Even above 8 km AGL, the umax50 storm does not exhibit larger rime growth rates than the other storms, although it does feature enhanced rime conversion between 6 and 8 km that may contribute to increasing hail mass. However, given these rates are
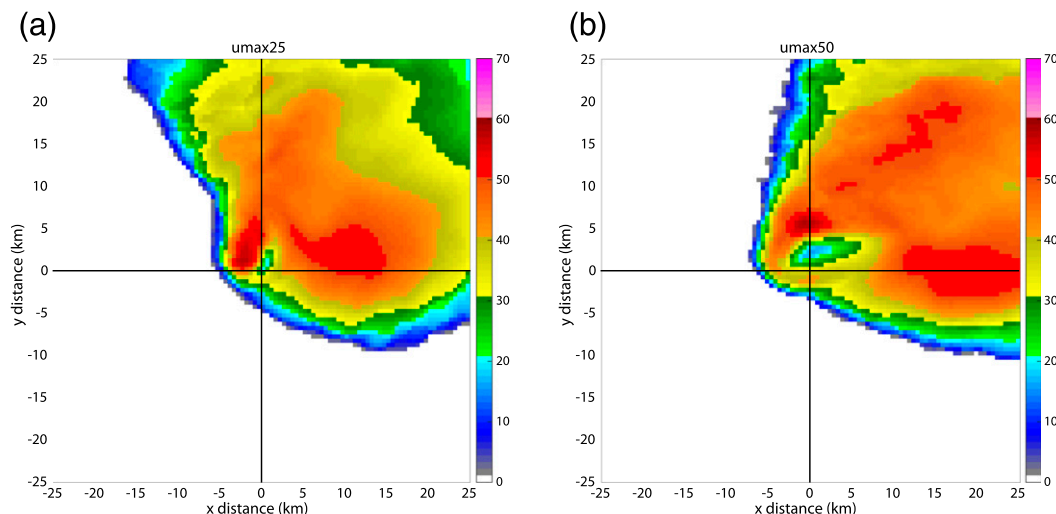
FIG. 6. Horizontal cross sections of simulated reflectivity factor (dBz; shaded according to scale) at 5.125 km AGL for the composites of the (a) umax25 and (b) umax50 storms. The black lines indicate where vertical cross sections are taken in subsequent figures.

an order of magnitude less than the rime growth and that it is not present in other storms, it is likely a secondary effect. Similarly, each storm's conversion rates overlap (Figs. 5b,c). Thus, it seems unlikely that differences in the average microphysical process rates are a major contributing factor to the observed differences in hail formation and growth aloft.

If the magnitudes of the process rates are not the main cause of hail production differences, then it could be the differences in updraft volume or hailstone residence time within the updraft; even if the average conversion rate and growth rate values are the same among the different storms, a larger growth region could lead to more hail production as these process rates act over a greater volume of the storm, and/or hailstones remaining in the growth region for longer periods of time could lead to larger hail mass. Recall that previous observational and modeling studies suggest that broader updrafts are more conducive to hail growth (e.g., Nelson 1983; Foote 1984; Picca and Ryzhkov 2012). Specifically, a broad region of moderate updraft allows hailstones to remain balanced in a region of efficient growth for a longer amount of time.

To investigate these differences, we first inspect the three-dimensional storm structures. Figure 6 shows a horizontal cross section of simulated reflectivity factor Z_H (a direct model output variable, based on the Rayleigh approximation to electromagnetic scattering) through the composite umax25 and umax50 storms at 5.125 km AGL. These storms are chosen to illustrate the two extremes of the subset of storms considered thus far. A semicircular bounded weak echo region (BWER) is evident in the umax25 storm (Fig. 6a), with a high-Z_H

core to its northwest. Vertical cross sections are taken through the center of the composite (updraft maximum at 6.125 km AGL) to explore the vertical structure of the storm (Figs. 7a,b). The storm exhibits a robust, vertically erect updraft. Below 8 km, substantial liquid mass mixing ratio is evident in a column on the western flank of the storm, as are maxima in the process rates (Fig. 7a, just west of 0 km). This is consistent with the findings of GvdH14 for "classic" supercells. Above this level, a maximum in freeze conversion caps the liquid mass mixing ratio contours, and rime growth contours are found throughout the updraft. Above 6 km, the process rates tend to favor the south flank of the updraft, just inside the Z_H echo overhang (Fig. 7b).

In contrast, the umax50 storm exhibits an elongated, well-defined BWER at midlevels (Fig. 6b), with an enclosed region of $Z_H < 30$ dBz stretching more than 5 km in the east–west direction. Vertical cross sections through this storm (Figs. 7c,d) exhibit similar structures to the umax25 storm, especially in the north–south plane. However, the most striking difference is the much larger horizontal extent of the updraft region in the umax50 storm in the east–west direction (Fig. 7c). For example, at 5.125 km AGL, the umax25 storm's updraft region bounded by the 20 m s^{-1} contour is approximately 5 (6.5) km wide in the east–west (north–south) direction, whereas the umax50 storm's is 11 (7) km wide. Clearly, the greater shear promotes a broader updraft in the direction of the enhanced shear vector. Rather than being tilted more downshear, the umax50 storm's updraft appears to be vertically erect, consistent with the discussion in Markowski and
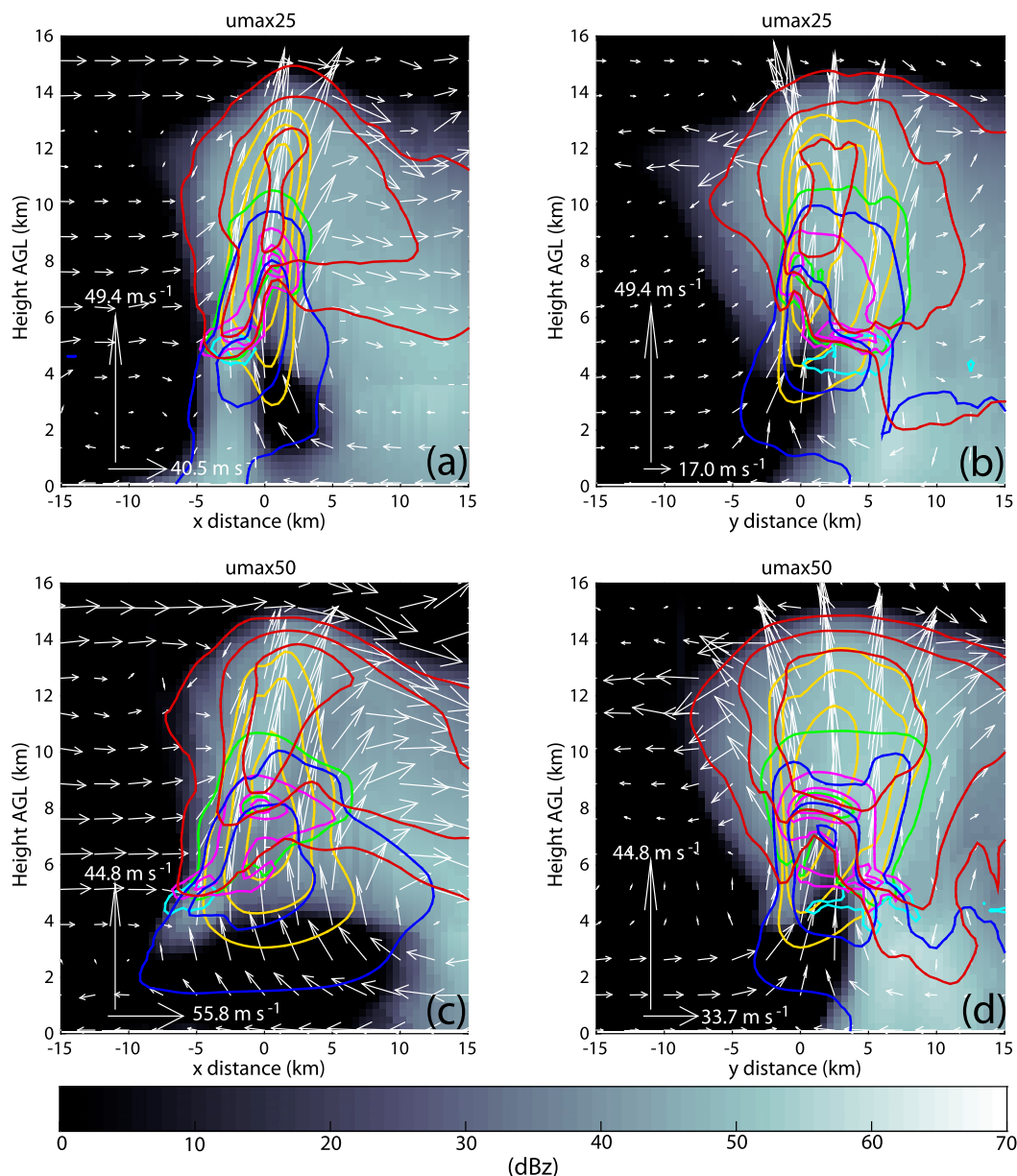
FIG. 7. Vertical cross section through the composite umax25 storm along the (a) east–west and (b) north–south directions. (c),(d) As in (a) and (b), respectively, but for the umax50 case. Grayscale shading is simulated reflectivity factor (dBz); white vectors are the two-dimensional winds in the plane of the cross section, with vector maxima in the lower left of each panel; blue contours are liquid (cloud and rain) drop mass mixing ratio (0.001, 0.005, and 0.01 kg kg^{-1}); blood red is hail mass mixing ratio (0.001, 0.005, and 0.01 kg kg^{-1}); chartreuse is rime growth (0.1, 1.0, and 2.0 $\times$ 10^{-4} kg kg^{-1} s^{-1}); cyan is rime conversion (0.1, 1.0, and 2.0 $\times$ 10^{-5} kg kg^{-1} s^{-1}); magenta is freeze conversion (0.1, 1.0, and 2.0 $\times$ 10^{-4} kg kg^{-1} s^{-1}); and updraft (20, 30, and 40 m s^{-1}) contours are goldenrod.

Richardson (2010) of how large vertical shear can promote upright updrafts (see also Rotunno et al. 1988). This elongated updraft also potentially serves to increase the volume over which microphysical processes act to increase hail mass and number concentration.

To quantify the impact of this larger updraft on process rates, we look at volumes in the domain (for the right-moving supercell only) in which process rates exceed certain thresholds: 6 $\times$ 10^{-5} kg kg^{-1} s^{-1} for rime growth and freeze conversion, and 6 $\times$ 10^{-6} kg kg^{-1} s^{-1} for rime conversion. These thresholds were chosen to ensure that smaller values associated with secondary convection or the left-moving supercell, which could spuriously increase volumes, are not included. Figure 8
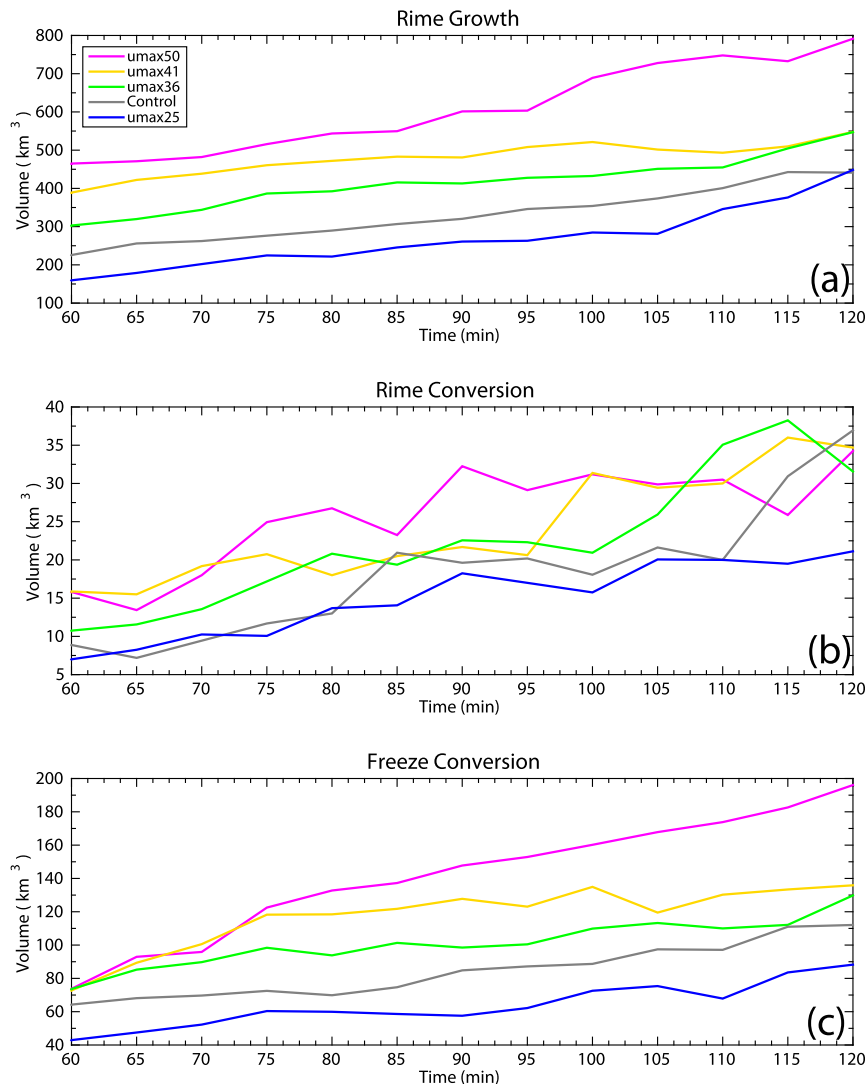
FIG. 8. Volumes of different process rates exceeding specified thresholds for the u_{max} storms. (a) Rime growth exceeding 6×10^{-5} kg kg^{-1} s^{-1}, (b) rime conversion exceeding 6×10^{-6} kg kg^{-1} s^{-1}, and (c) freeze conversion exceeding 6×10^{-5} kg kg^{-1} s^{-1}. Colors indicate simulations as in previous figures. Note the different ordinate axes used in each panel.

shows the time series of these volumes for the simulated storms. For rime growth (Fig. 8a), the storms exhibit a clear separation, with high-shear storms displaying larger volumes throughout the time period shown. By the end of the simulation, the umax50 storm exhibits nearly twice the volume of rime growth exceeding the chosen threshold than the umax25 storm. The relationship for rime conversion (Fig. 8b) is not as clear, though for much of the time period the general trend is for the higher-shear cases to have larger volumes than the lower-shear cases. Freeze conversion (Fig. 8c) again exhibits a clear separation throughout most of the time period, with umax50 exhibiting more than twice the

volume exceeding the chosen threshold as umax25 by the end of the simulation.

These results, when considering the similar overall magnitudes of the process rates, imply that increased u-component deep-layer shear causes *broader* updrafts (elongated in the west–east direction), in which larger volumes of optimal growth conditions occur. It is not the magnitudes of the process rates or the updraft speed that seems to be most important for hail growth in this subset of simulations but, rather, the volume in which optimal growth conditions exist. This is consistent with previous studies that suggested broad updrafts are conducive to hail growth (e.g., Nelson 1983).
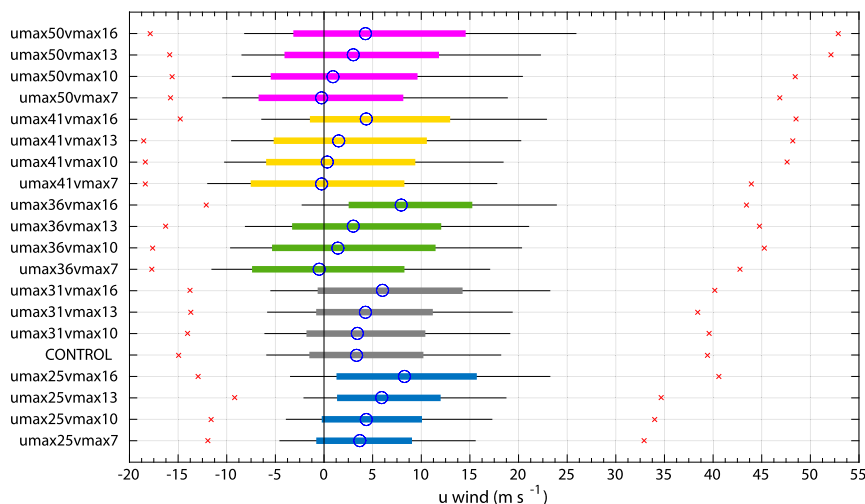
FIG. 9. Box-and-whisker plots showing distributions of storm-relative u-wind components in the hail growth region ($w > 20\ \mathrm{m\,s^{-1}}$; 5.125–8.625 km AGL) from the composites of each storm. The blue circle is the median value, the colored box is the 25th–75th-percentile (interquartile) range, the whiskers extend from the 10th- to 90th-percentile range, and the red crosses indicate the maximum and minimum values.

Investigating hailstone residence time within the prime hail growth region is more difficult, as the bulk microphysics model does not explicitly predict individual hailstones or their trajectories through the storm. Instead, we take the distribution of storm-relative u and v winds in the hail growth region to determine if hailstones *would* spend more time in the updraft. Distributions are constructed for values within updraft regions $>20\ \mathrm{m\,s^{-1}}$ between 5.125 and 8.625 km AGL, which corresponds to environmental temperatures from $-9.5°$ to $-33°C$. Figures 9 and 10 show these distributions. Although increasing $u_{\max}$ tends to increase the maximum storm-relative u-wind values within the

updraft, the medians are shifted toward lower values (Fig. 9). Overall, storm-relative v-wind magnitudes do not change much with increasing $u_{\max}$. The large increase in updraft size and decrease in updraft intensity with increasing east–west shear probably dominate these slight increases in storm-relative u- and v-wind extrema within the updraft, leading to enhanced residence time for hailstones passing through the growth region. However, this enhanced resonance time is probably a secondary effect to the increased volume.

In summary, this subset of simulations provides strong evidence that environmental wind shear plays a significant role in modulating the hail production in supercell
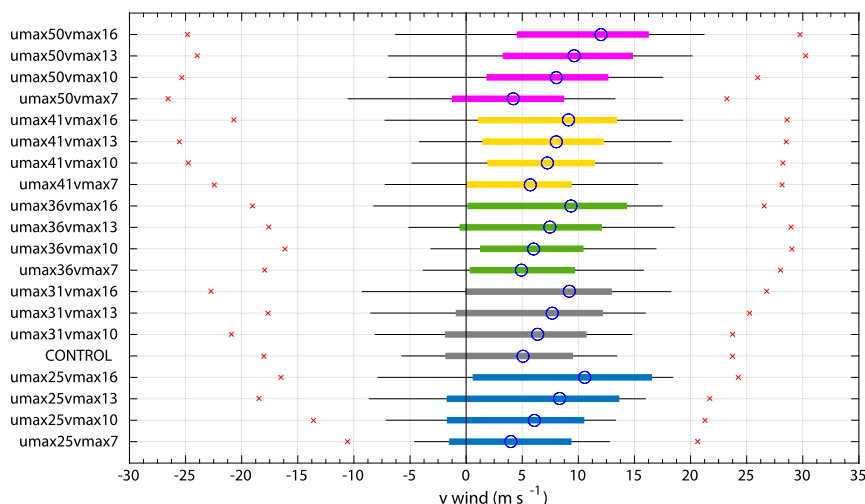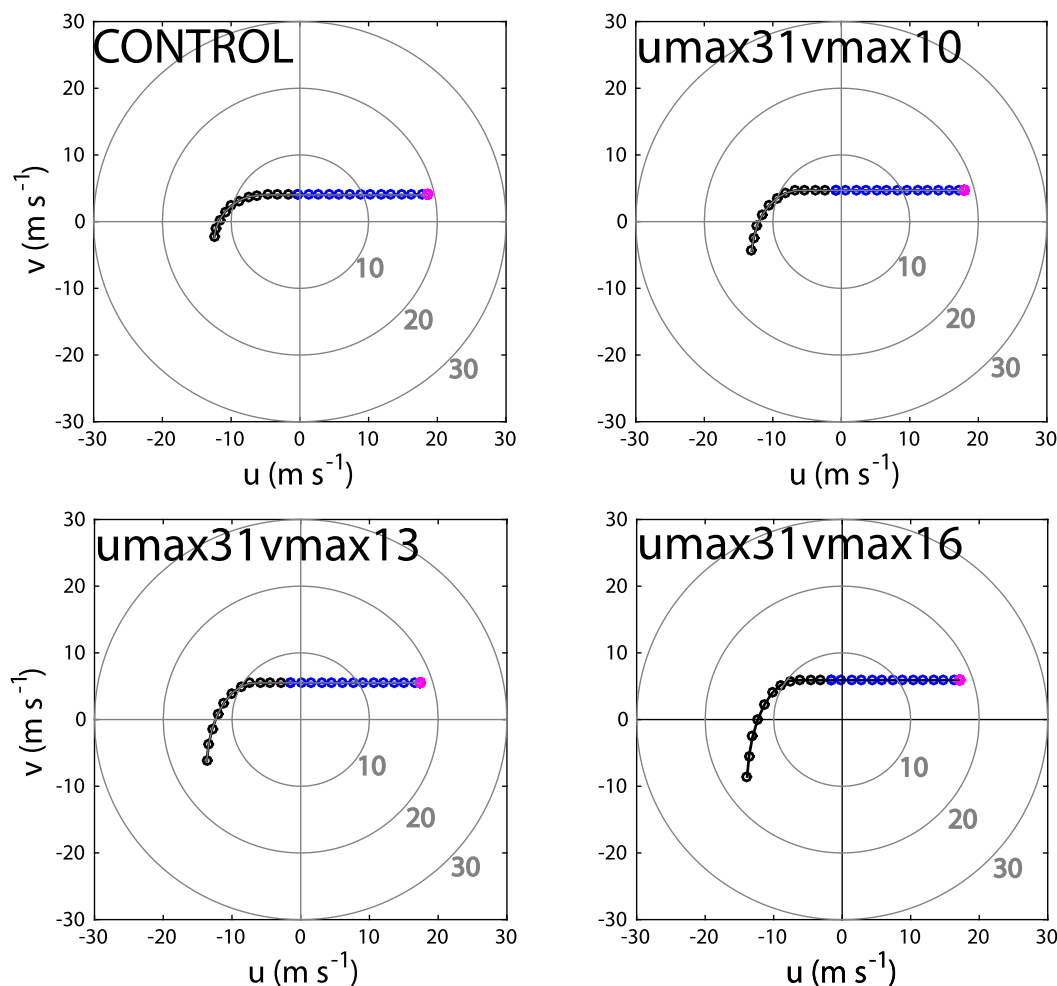

FIG. 10. As in Fig. 9, but for the storm-relative v component.

FIG. 11. As in Fig. 1, but for the v_{max} cases.

storms. In particular, enhanced u-component (deep layer) shear leads to updrafts elongated in the direction of the shear vector. Maximum updraft speeds are slightly less for increased deep-layer shear, which, when combined with these larger volumes and only slight increases in u and v storm-relative winds within the updraft, likely lead to longer residence times. The broader updrafts provide more volume over which hailstones may form (predominantly by freeze conversion), and, when combined with longer residence times, provide more volume and time in which hailstones may grow (predominantly by accretion of supercooled cloud and rainwater).

b. The v-component cases

In this subsection, we present a subset of simulations in which the v component of shear is altered. Recall that the v shear occurs over the lowest 3 km of the troposphere for the idealized hodographs used herein.

Enhancements in low-level north–south shear may be associated with a nocturnal low-level jet, for example. In typical supercell environments, the magnitude of this north–south shear is much less than the east–west shear, given the predominantly westerly flow across midlatitudes.

These simulations vary the v_{max} parameter from the control value ($7 \, m \, s^{-1}$) to 10, 13, and $16 \, m \, s^{-1}$ for each of the u_{max} values presented above. The associated hodographs for the cases with $u_{max} = 31 \, m \, s^{-1}$ are shown in Fig. 11. Note that, for a given u_{max} value, increasing v_{max} increases the 0–3-km storm-relative helicity (Table 1). Similar to the u_{max} cases, the maximum updraft speeds averaged over the last 40 min vary slightly [e.g., by only $4 \, m \, s^{-1}$ between the control (vmax7) and vmax16 cases; not shown]. Again, the higher-v-shear cases have slightly weaker average updrafts than the lower-v-shear cases.

Vertical profiles of average q_h for the v_{max} cases with $u_{max} = 31 \, m \, s^{-1}$ reveal heavy overlap between their 95%
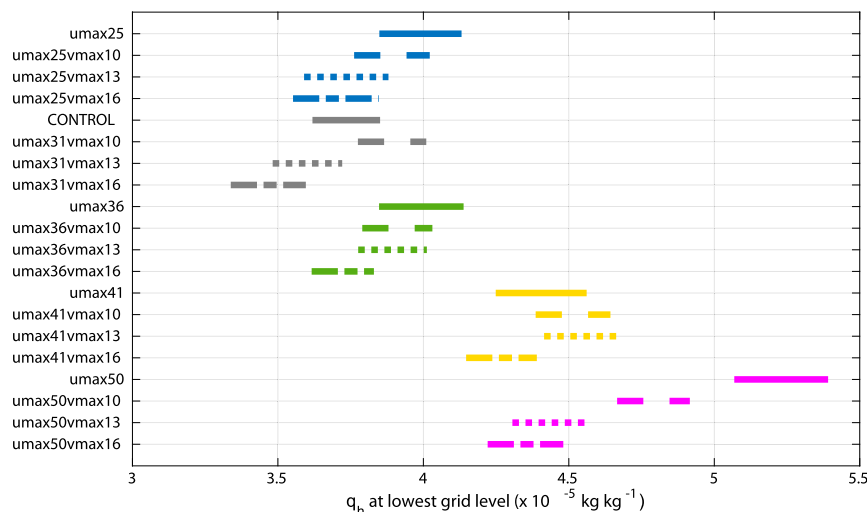
FIG. 12. The 95% confidence intervals about the average q_h at the lowest grid level for each composited storm. Each group of u_{max} storms is color coded as before; v_{max} storms within each u_{max} group are indicated by different dashed lines.

confidence intervals (not shown). This is perhaps unsurprising, given the relatively small changes in v_{max} values relative to those for the u_{max} cases. Surprisingly, however, the larger v_{max} values have smaller q_h at most levels, including the lowest grid level (Fig. 12). At that level, we do find a general trend that increasing v_{max} (low-level north–south shear) for a given u_{max} value tends to decrease the average q_h, which holds for most u_{max} values (Fig. 12). There is a statistically significant (at the 95% level) decrease in lowest-grid-level q_h when comparing the weakest v shear to the strongest shear within each u_{max} group except umax41. This decrease in hail mass for a $6 \, \mathrm{m \, s^{-1}}$ increase in v_{max} strongly contrasts the increase in hail mass seen for a $6 \, \mathrm{m \, s^{-1}}$ increase in u_{max}.

Similar to the u_{max} cases, the averaged vertical profiles of process rates do not show substantial differences; in fact, the spread between the different simulations is smaller in magnitude than for the u_{max} cases (not shown). Thus, we again turn to changes in storm structure to explain the observed differences in hail production.

To investigate the impact of the low-level v-shear changes on the updraft structure, we construct horizontal cross sections at midlevels ($5.625 \, \mathrm{km}$) for the subset of v-shear cases (Fig. 13). The control run (Fig. 13a) features a classic crescent-shaped updraft region and a well-defined BWER. The maxima in process rates are confined to the western edge of the updraft at this height. Similarly to the u_{max} storms, the storms with the enhanced low-level (v component) shear exhibit elongated updrafts in the direction of the shear vector (north–south in this case). As the v component of the

shear increases (Figs. 13b–d), the northern portion of the crescent-shaped updraft expands and extends westward. This is consistent with the better correlation of vertical velocity and vertical vorticity implied by the larger storm-relative helicity in these cases (e.g., Davies-Jones 1984; Weisman and Rotunno 2000; Table 1). Within the updraft there is also slightly larger storm-relative westerly (Fig. 9) and southerly momentum (Fig. 10) as the v-component shear is increased.

Similar to the u_{max} cases, increasing v-component shear tends to produce an increase in the volumes over which the process rates are active (Fig. 14). However, perhaps given the smaller relative changes in v-shear relative to u-shear cases, the differences between cases are not as pronounced. Thus, despite the larger updrafts and associated larger volumes over which microphysical processes are acting, increasing low-level north–south shear leads to *reductions* in hail production. To explain this behavior, we investigate possible pathways hailstones take through these storms.

c. Hailstone pseudotrajectories

As discussed in GvdH14, computing hailstone growth trajectories is not possible in bulk microphysics schemes. This is largely because bulk schemes predict only integrated moments of the distribution instead of individual sizes, and these moments can have different weighted fall speeds. Nonetheless, we can construct "pseudotrajectories" that provide some insights into plausible hail pathways through the storm using the composited fields (i.e., assuming steady-state average storm structure for these calculations). We prescribe
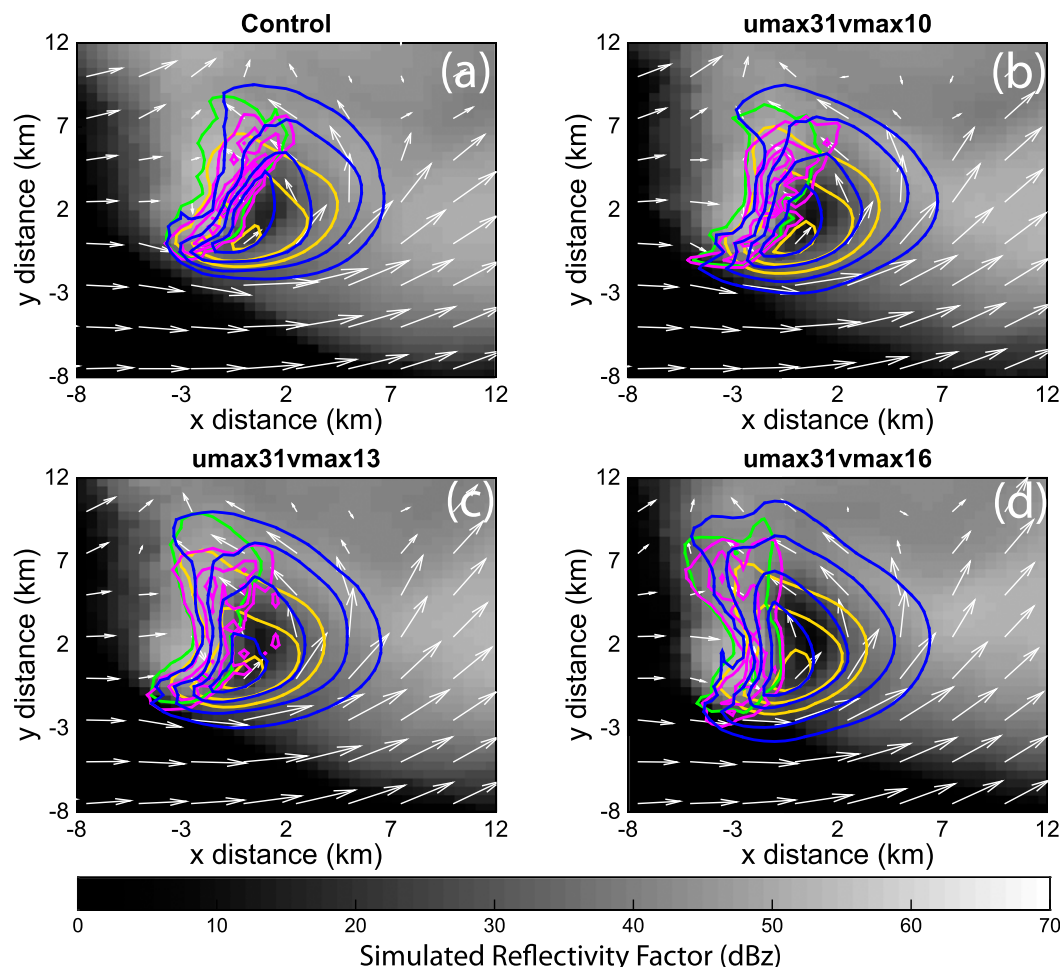
FIG. 13. Horizontal cross sections at 5.625 km AGL for the (a) control, (b) umax31vmax10, (c) umax31vmax13, and (d) umax31vmax16 cases. Grayscale shading is simulated reflectivity factor (dBz); white vectors are the two-dimensional winds within the plane of the cross section; blue contours are liquid (cloud and rain) drop mass mixing ratio (0.001, 0.005, and 0.01 kg kg^{-1}); chartreuse is rime growth (0.1, 1.0, and 2.0 × 10^{-4} kg kg^{-1} s^{-1}); magenta is freeze conversion (0.1, 1.0, and 2.0 × 10^{-4} kg kg^{-1} s^{-1}); and updraft (20, 30, and 40 m s^{-1}) contours are goldenrod.

embryo locations and sizes to initialize a pseudo-trajectory. Then, using a 1-s time step, these embryos are advected with the composited storm-relative u and v fields. Vertical motion is given by w minus the particle's fall speed, which is determined using the hail fall-speed relationship used in the Morrison two-moment scheme that is based on Matson and Huggins (1980). As the particles enter a region of hailstone growth (as determined by composited microphysical process rate fields), their growth is computed from the composited rime growth rate at that grid box. Throughout the growth, number mixing ratio is held constant at 10 kg^{-1}; though results are quantitatively sensitive to this choice, the qualitative trajectories and insights gained from them are the same. Similarly, though quantitative sensitivity was found for initial embryo sizes (which are

arbitrarily chosen based on realistic observed embryo sizes), the qualitative results remain unchanged. Hailstone sizes predicted by these pseudotrajectories should not be taken literally but do show which trajectories encounter larger growth rates, which we can take as a proxy for larger sizes. The calculations are terminated when the hailstones reach the lowest grid level or exit through other domain boundaries. No melting is considered in these calculations.

Though these are an approximation for real hailstone growth trajectories, some confidence in their plausibility is given by their similarity to those found in previous studies (e.g., Nelson 1983; Foote 1984; Miller et al. 1990). Further, the trajectories reach the ground within reflectivity contours and regions of nonzero q_h. An example of such a trajectory is shown in Fig. 15. In this
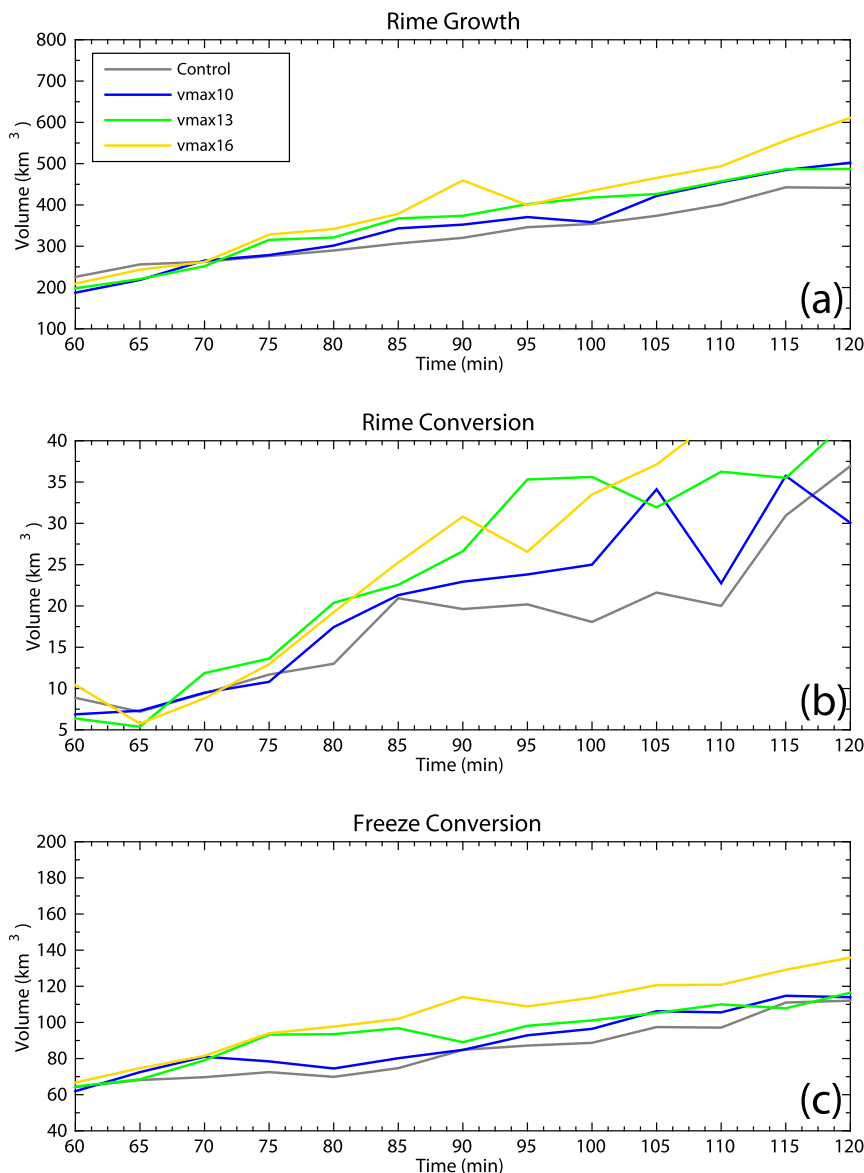
FIG. 14. As in Fig. 8, but for the $v_{\max}$ storms. Gray curves indicate the control run, blue curves indicate vmax10, green curves indicate vmax13, and goldenrod curve indicate vmax16.

example trajectory, a 2-mm-diameter embryo is initiated aloft on the right (south) flank of the updraft (green circle), in a region prior studies have called the "embryo curtain" or "embryo corridor." The particle falls cyclonically around the updraft (red isosurface = $20 \, \mathrm{m \, s^{-1}}$), where it is reingested at the base on the front (east) side. Thereafter, it quickly ascends and grows rapidly. Its arching trajectory passes inside the 45-dBz isosurface (yellow), grazing the edge of the so-called reflectivity "vault." After reaching its apex, it falls out of the updraft and reaches the surface north of the low-level mesocyclone as an 18.8-mm stone. This pathway is

consistent with the hypothesized trajectories of Browning and Foote (1976) and simulated trajectories in Foote (1984) and others discussed in the introduction.

For each composited storm, we seed 2-mm embryos at every grid box within the domain for heights from 4.875 to 11.125 km AGL. Though not each of these initial locations is realistic, the resulting calculations show *which of these locations result in significant hailstone growth*. These potential embryo initial locations can then be compared to the actual locations of hydrometeors in the simulated storms to assess whether the embryos could be realized (i.e., if hydrometeors are unavailable in a
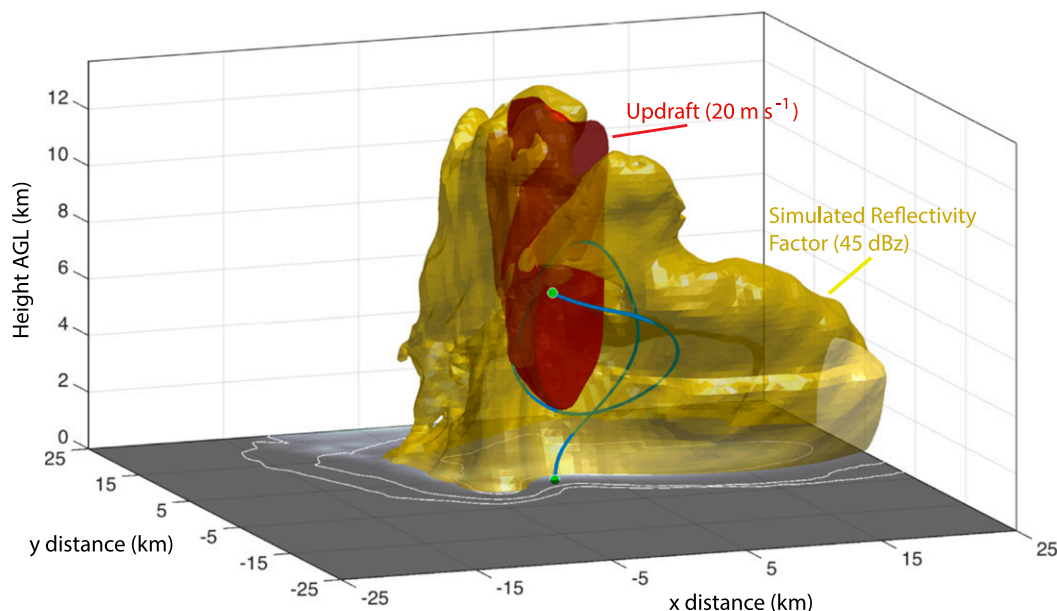
FIG. 15. Simulated hailstone pseudotrajectory (blue line) initialized as a 2-mm embryo (green circle). Updraft 20 m s^{-1} (red) and simulated reflectivity factor 45-dBz (yellow) isosurfaces are shown. White contours at the surface show 30-, 40-, and 50-dBz reflectivity factor at the lowest model grid level.

region favorable for embryos to grow, the growth is not realized for that case).

Figure 16 shows examples of such calculations for the control simulation. Each panel shows embryos initialized at a particular height. At each height, the embryo initial locations are shaded by the final size attained by that embryo at the lowest grid level (recall that melting is not accounted for in these calculations). The darker-shaded regions indicate that embryos initialized at those locations undergo significant growth during their path through the storm. Figure 16 reveals several important embryo source regions that lead to significant hail growth. First, at lower levels, the right (southern) flank of the storm reveals a region for preferred growth that shifts rearward to the western flank of the storm with increasing height. This is the *embryo curtain* discussed in numerous previous studies (e.g., Browning and Foote 1976). Its consistency with previous work provides confidence in our pseudotrajectories. Aloft, there is a narrow band of locations west of the updraft that also results in substantial hail growth. Finally, embryos within the updraft below 8 km (Figs. 16a–c) are in favorable locations for significant growth. In real supercells, such embryos would be frozen raindrops, supplied from below in the region observed with polarimetric radar called the "Z_{DR} column" (e.g., Kumjian et al. 2014, and references therein). Such frozen drop embryos often are found in real hailstones (e.g., Knight 1981; Rasmussen and Heymsfield 1987).

The embryo curtain or corridor on the south flank of the updraft is partially located within simulated reflectivity contours, suggesting that hydrometeors are present at these locations and may participate in hail growth. However, portions of the embryo corridor (especially aloft) are found outside these reflectivity contours. This implies that these potential embryo pathways are not realized by the simulated storm because there are no hydrometeors present there.

Figure 17 shows the same type of calculations for the umax50 storm. The three main starting locations for embryos are evident in this storm, similar to those in the control run. However, the embryo corridor region is elongated in the direction of the shear vector, similar to the updraft. This provides a broader region of initial embryo locations that can result in significant growth. For example, the umax50 storm has nearly 20% more grid boxes of initial embryo locations that start in regions of $Z_H > 0 \text{ dB}z$ that result in final hailstone sizes >10 mm. Thus, in addition to broader updrafts, enhanced zonal (deep layer) shear results in a larger source volume for hailstone embryos.

In contrast, enhancing the low-level meridional shear for the umax50vmax16 actually *decreases* the source region for embryos compared to the umax50 case (Fig. 18). The stronger southerly storm-relative winds serve to decrease the hail production by two combined effects. First, hydrometeors that could serve as potential embryos are advected farther north by the stronger
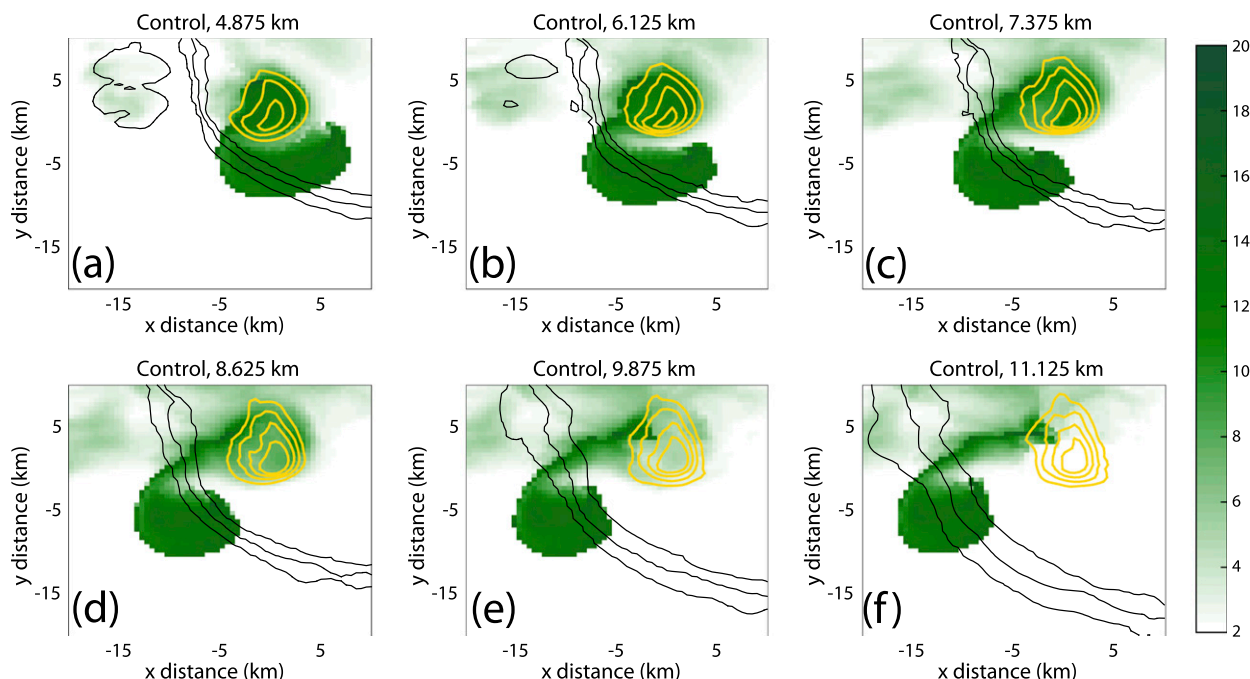
FIG. 16. Initial embryo locations at different heights, shaded by the final hailstone diameter at the surface (according to scale; mm) for the control simulation. Simulated reflectivity factor -20-, -10-, and 0-dBz contours at that height are overlaid (black), as are 10, 20, 30, and 40 m s^{-1} updraft contours (goldenrod). Shading outside the black (reflectivity) contours indicates that simulated hydrometeors are unavailable at those locations, and thus the initial embryo locations favorable for growth are not realized.

southerly storm-relative winds, resulting in a lack of embryos in the potentially favorable region (i.e., notice the ~5-km northward shift of the simulated reflectivity contours from umax50 to umax50vmax16; cf. Figs. 17 and 18). Second, the potentially favorable embryo region is shifted southward, as embryos now take longer northward paths before entering the updraft (cf. Figs. 17a and 18a). In this way, the region of potentially favorable embryo initial locations is separated from the supply region of actual hydrometeors. Thus, increased low-level north–south shear reduces the potential embryo source regions in the embryo corridor.

4. Discussion and summary

To investigate the impact of vertical wind shear on hail growth in supercell storms, a series of idealized supercell simulations is performed in which the thermodynamic profile is held constant and the hodograph is systematically altered. Our results show that changes in the environmental hodograph affect the shape, size, and strength of the updraft in simulated supercell storms. This has significant impacts on the hail produced in a given idealized supercell. Composite fields over the last hour of simulation time for each case were constructed to robustly compare structural differences among the different storms.

Increasing the u-component shear in the hodograph, which is equivalent to increasing deep-layer shear, leads to an elongated updraft in the east–west direction. This leads to statistically significant increases in hail mass mixing ratio with increasing shear. Though the magnitudes of the Morrison two-moment microphysical scheme process rates relevant to hail production (grouped into conversion by freezing, conversion by riming, and riming growth) are not significantly different among the different simulations, the increased volume of updrafts over which these process rates contribute to hail growth leads to the observed correlation between hail production and deep-layer zonal shear. As a secondary effect, the broader, weaker updrafts and insignificantly changed horizontal flow within the updrafts may contribute to larger residence times for hailstones. Increasing the v-component shear, which is the north–south shear in the lowest 3 km AGL, similarly leads to an elongation of the updraft in the north–south direction. However, unlike the u-component shear cases, increasing the low-level meridional shear for a given amount of zonal shear tends to decrease the hail mass mixing ratio.

To determine why, hailstone growth pseudotrajectories were constructed from the composited fields. These pseudotrajectories reveal three main embryo source
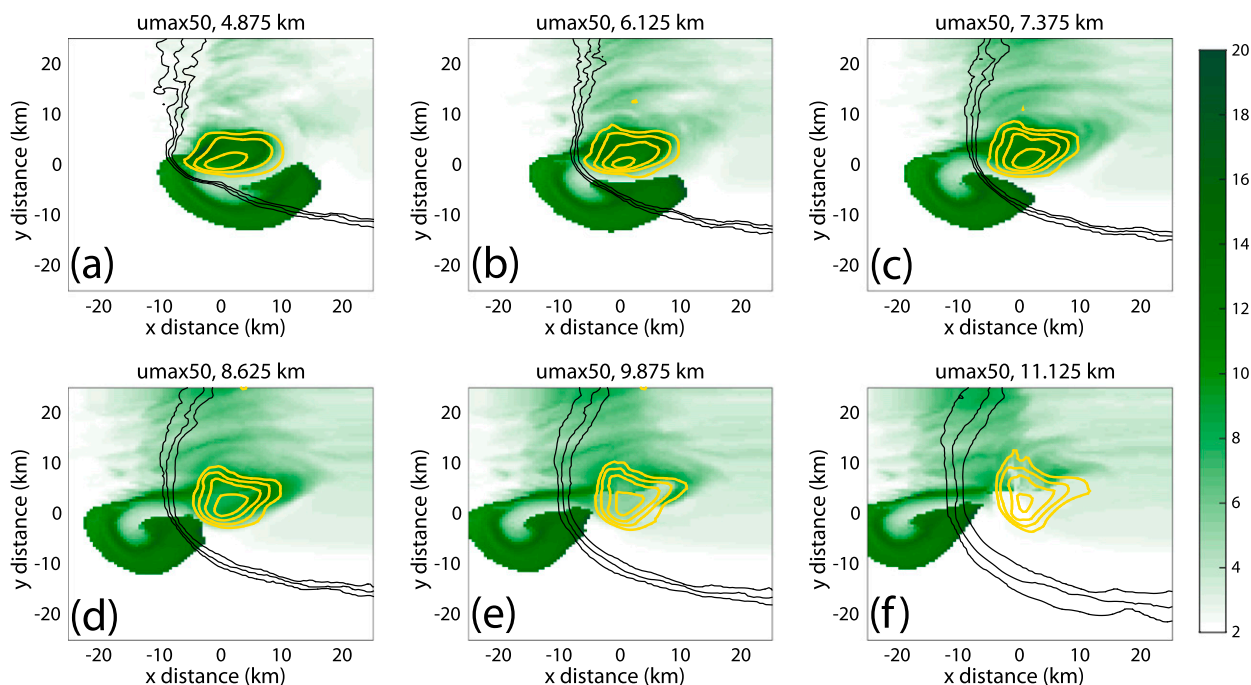
FIG. 17. As in Fig. 16, but for the umax50 storm. Note the expanded axes.

regions that are consistent with prior studies: (i) the right (south) flank of the updraft, a region known as the embryo corridor; (ii) a narrow ribbon along the rear (west) flank of the updraft aloft; and (iii) within the updraft below 8 km AGL. Increased deep-layer (west–east) shear broadened the embryo source regions (particularly the embryo corridor and the updraft), resulting in a larger volume of the storm over
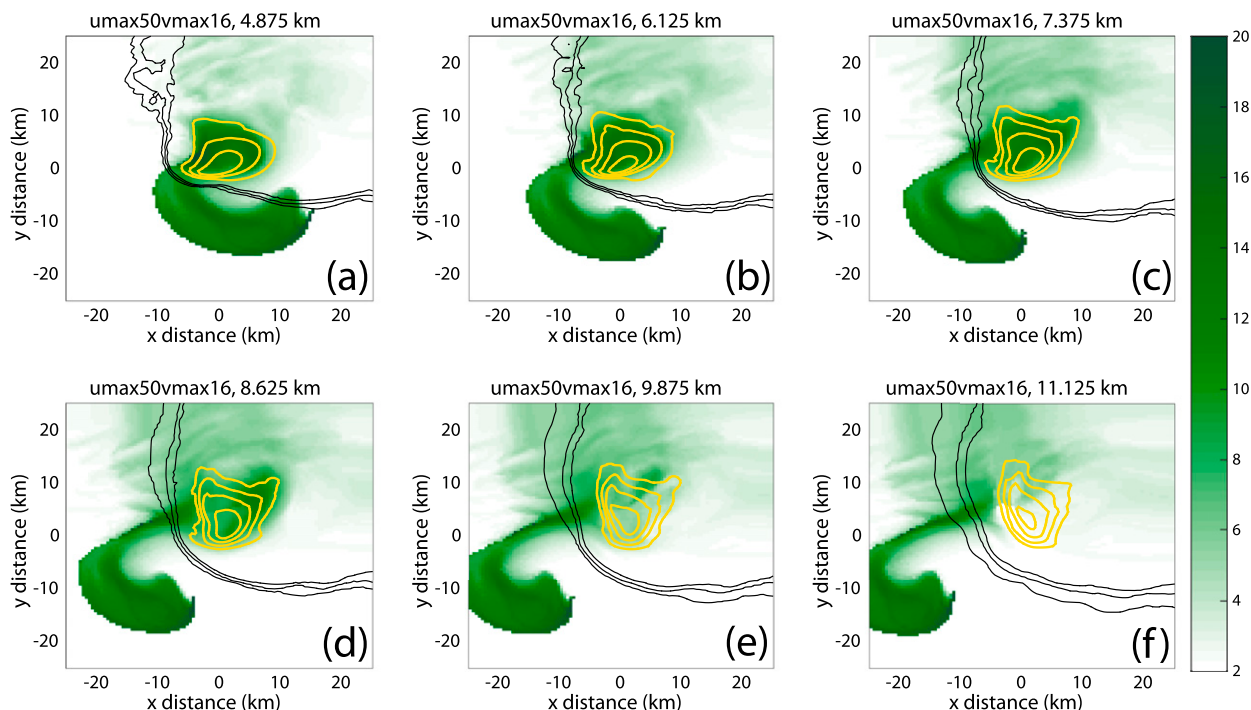

FIG. 18. As in Fig. 17, but for the umax50vmax16 storm.

which hydrometeors could start paths that result in substantial growth. However, increased low-level (south–north) shear reduces embryo sources by shifting the embryo corridor southward and shifting hydrometeors that can seed the embryo corridor northward, resulting in minimal overlap between the supply region of actual hydrometeors and the potential initial locations that would lead to significant growth.

In both sets of simulations, increasing shear leads to an elongation of the updraft along the direction of the shear vector. Though our model output fields are insufficient to diagnose the reasons for this elongation, we speculate on two possibilities. First, because the horizontal gradients of vertical velocity on the upshear side of the storm are not significantly different among the different simulations, increased shear would promote larger perturbation pressure gradients across the updraft in the direction of the shear vector (e.g., Rotunno and Klemp 1982, 1985; Markowski and Richardson 2010). This could lead to larger horizontal accelerations for parcels ascending in the main updraft. Second, the enhanced shear case has larger horizontal storm-relative winds within the updraft (Figs. 9, 10), leading to more lateral displacement as parcels ascend. Additional idealized modeling studies in a simplified framework (e.g., dry convection) could provide a more rigorous explanation for this observed behavior.

Clearly, the simulations used herein are highly idealized, and real cases may have substantially different hodograph shapes. However, we opted for the simple quarter-circle hodograph to facilitate a systematic exploration of the parameter space. Thus, a natural question arises: how representative are these results of real cases in which hodographs may be more complex? Though observational studies are limited and beyond the scope of this paper, a recent study by Johnson and Sugden (2014) shows composited hodographs for different size classes of surface hail reports. Based on their cases, a trend can be seen for larger hail reports to be associated with hodographs elongated in the east–west direction. In other words, deep-layer u-component shear was correlated with reports of larger hail size. This observational study thus appears to be broadly consistent with our idealized modeling results.

The results of our study open an avenue for future research that could potentially lend skill to operational severe weather forecasting. Identifying environmental controls favorable for large-hail production given an environment otherwise favorable for convective storms could allow for improved assessment of the conditional large-hail threat. However, spectral bin microphysics treatments are necessary to understand environmental impacts on the surface hail size distribution, which is of

chief operational concern. Although suppression is not a major focus of research today, the ability to forecast hail events can allow movement of assets (e.g., cars, aircraft, and people) in advance of storms, potentially reducing damage, and thus reducing cost. Also, anticipation of major hail days will allow insurance companies to staff adequate numbers of claims adjusters.

Some studies (e.g., Nelson 1987; Kumjian and Ryzhkov 2008) have suggested that nontornadic supercell storms are more prolific large-hail producers than tornadic ones. Our finding that increasing v-component (low level) shear for a given amount of deep-layer u-component shear tends to decrease hail production may be consistent with these suggestions; increased v-component shear at low levels is associated with increases in storm-relative helicity. Further, for the hodographs considered in this study with similar lengths, the one with larger 0–3-km storm-relative helicity tends to have less hail at the surface. All else being equal, hodographs with greater low-level curvature and/or larger low-level storm-relative helicity would tend to be more favorable for tornadogenesis (e.g., Rasmussen and Blanchard 1998; Thompson et al. 2003, 2007). We speculate that hodographs supportive of tornadic supercells are less supportive for large-hail production because of the changes in storm structure and embryo source regions identified in this study. Thus, it is not simply the total hodograph length (or total shear) that is important for hail production, but rather how it is partitioned, reminiscent of the findings of McCaul and Weisman (2001) for supercell intensity and structure.

The idealized simulations performed herein only occupy a portion of the possible parameter space. As such, this study should be seen as a first step toward exploring the role vertical wind shear plays on controlling hail growth. A remaining question is how melting responds to these environmental changes, given that melting plays a large role in modulating the hail size distribution reaching the surface. Limitations of two-moment schemes like the one used herein prevent a rigorous treatment of this question; future work involving more sophisticated bin microphysics is needed to adequately address the problem of melting and the resultant surface hail size distributions. Future efforts should also expand on the parameter space, using more realistic hodograph shapes and/or hodographs from real cases, as well as investigating how different combinations of CAPE and shear affect hail production. For example, the results found herein should be validated for different thermodynamic environments. In addition to providing insights into controls on hail growth, such studies can improve our basic understanding of how environmental factors affect updraft size. Future studies should use more detailed microphysical treatments

(e.g., spectral bin models) to explore the impacts of these environmental factors on hailstone sizes and size distributions reaching the surface to better understand the nature of a given event's potential hail risk.

REFERENCES

Brooks, H. E., C. A. Doswell, and R. B. Wilhelmson, 1994: The role of midtropospheric winds in the evolution and maintenance of low-level mesocyclones. *Mon. Wea. Rev.*, **122**, 126–136, doi:10.1175/1520-0493(1994)122<0126:TROMWI>2.0.CO;2.

Browning, K. A., 1964: Airflow and precipitation trajectories with severe local storms which travel to the right of the winds. *J. Atmos. Sci.*, **21**, 634–639, doi:10.1175/1520-0469(1964)021<0634:AAPTWS>2.0.CO;2.

——, and G. B. Foote, 1976: Airflow and hail growth in supercell storms and some implications for hail suppression. *Quart. J. Roy. Meteor. Soc.*, **102**, 499–533, doi:10.1002/qj.49710243303.

Bryan, G. H., and J. M. Fritsch, 2002: A benchmark simulation for moist nonhydrostatic numerical models. *Mon. Wea. Rev.*, **130**, 2917–2928, doi:10.1175/1520-0493(2002)130<2917:ABSFMN>2.0.CO;2.

Conway, J. W., and D. S. Zrnić, 1993: A study of embryo production and hail growth using dual-Doppler and multiparameter radars. *Mon. Wea. Rev.*, **121**, 2511–2528, doi:10.1175/1520-0493(1993)121<2511:ASOEPA>2.0.CO;2.

Davies-Jones, R. P., 1984: Streamwise vorticity: The origin of updraft rotation in supercell storms. *J. Atmos. Sci.*, **41**, 2991–3006, doi:10.1175/1520-0469(1984)041<2991:SVTOOU>2.0.CO;2.

Dawson, D. T., M. Xue, J. A. Milbrandt, and M. K. Yau, 2010: Comparison of evaporation and cold pool development between single-moment and multimoment bulk microphysics schemes in idealized simulations of tornadic thunderstorms. *Mon. Wea. Rev.*, **138**, 1152–1171, doi:10.1175/2009MWR2956.1.

——, E. R. Mansell, Y. Jung, L. J. Wicker, M. R. Kumjian, and M. Xue, 2014: Low-level Z_{DR} signatures in supercell forward flanks: The role of size sorting and melting of hail. *J. Atmos. Sci.*, **71**, 276–299, doi:10.1175/JAS-D-13-0118.1.

Efron, B., and R. J. Tibshirani, 1993: *An Introduction to the Bootstrap*. 1st ed. Chapman and Hall, 456 pp.

Foote, G. B., 1984: A study of hail growth utilizing observed storm conditions. *J. Climate Appl. Meteor.*, **23**, 84–101, doi:10.1175/1520-0450(1984)023<0084:ASOHGU>2.0.CO;2.

——, and C. A. Knight, 1979: Results of a randomized hail suppression experiment in northeast Colorado. Part I: Design and conduct of the experiment. *J. Appl. Meteor.*, **18**, 1526–1537, doi:10.1175/1520-0450(1979)018<1526:ROARHS>2.0.CO;2.

Grant, L. D., and S. C. van den Heever, 2014: Microphysical and dynamical characteristics of low-precipitation and classic supercells. *J. Atmos. Sci.*, **71**, 2604–2624, doi:10.1175/JAS-D-13-0261.1.

Heymsfield, A. J., 1983: Case-study of a hailstorm in Colorado. Part IV: Graupel and hail growth mechanisms deduced through particle trajectory calculations. *J. Atmos. Sci.*, **40**, 1482–1509, doi:10.1175/1520-0469(1983)040<1482:CSOAHI>2.0.CO;2.

Johnson, A. W., and K. E. Sugden, 2014: Evaluation of sounding-derived thermodynamic and wind-related parameters associated with large hail events. *Electron. J. Severe Storms Meteor.*, **9** (5). [Available online at http://www.ejssm.org/ojs/index.php/ejssm/article/viewArticle/137.]

Kalina, E. A., K. Friedrich, H. Morrison, and G. H. Bryan, 2014: Aerosol effects on idealized supercell thunderstorms in different environments. *J. Atmos. Sci.*, **71**, 4558–4580, doi:10.1175/JAS-D-14-0037.1.

Kennedy, P. C., and A. G. Detwiler, 2003: A case study of the origin of hail in a multicell thunderstorm using in situ aircraft and polarimetric radar data. *J. Appl. Meteor.*, **42**, 1679–1690, doi:10.1175/1520-0450(2003)042<1679:ACSOTO>2.0.CO;2.

Klemp, J. B., and D. K. Lilly, 1978: Numerical simulation of hydrostatic mountain waves. *J. Atmos. Sci.*, **35**, 78–107, doi:10.1175/1520-0469(1978)035<0078:NSOHMW>2.0.CO;2.

——, and R. Wilhelmson, 1978: The simulation of three-dimensional convective storm dynamics. *J. Atmos. Sci.*, **35**, 1070–1096, doi:10.1175/1520-0469(1978)035<1070:TSOTDC>2.0.CO;2.

Knight, C. A., G. B. Foote, and P. W. Summers, 1979: Results of a randomized hail suppression experiment in northeast Colorado. Part IX: Overall discussion and summary in the context of physical research. *J. Appl. Meteor.*, **18**, 1629–1639, doi:10.1175/1520-0450(1979)018<1629:ROARHS>2.0.CO;2.

Knight, N. C., 1981: The climatology of hail embryos. *J. Appl. Meteor.*, **20**, 750–755, doi:10.1175/1520-0450(1981)020<0750:TCOHE>2.0.CO;2.

Kumjian, M. R., and A. V. Ryzhkov, 2008: Polarimetric signatures in supercell thunderstorms. *J. Appl. Meteor. Climatol.*, **47**, 1940–1961, doi:10.1175/2007JAMC1874.1.

——, and ——, 2012: The impact of size sorting on the polarimetric radar variables. *J. Atmos. Sci.*, **69**, 2042–2060, doi:10.1175/JAS-D-11-0125.1.

——, A. P. Khain, N. BenMoshe, E. Ilotoviz, A. V. Ryzhkov, and V. T. J. Phillips, 2014: The anatomy and physics of Z_{DR} columns: Investigating a polarimetric radar signature with a spectral bin microphysical model. *J. Appl. Meteor. Climatol.*, **53**, 1820–1843, doi:10.1175/JAMC-D-13-0354.1.

——, Z. J. Lebo, and H. C. Morrison, 2015: On the mechanisms of rain formation in an idealized supercell storm. *Mon. Wea. Rev.*, **143**, 2754–2773, doi:10.1175/MWR-D-14-00402.1.

Lebo, Z. J., 2014: The sensitivity of a numerically simulated idealized squall line to the vertical distribution of aerosols. *J. Atmos. Sci.*, **71**, 4581–4596, doi:10.1175/JAS-D-14-0068.1.

——, H. Morrison, and J. H. Seinfeld, 2012: Are simulated aerosol-induced effects on deep convective clouds strongly dependent on saturation adjustment? *Atmos. Chem. Phys.*, **12**, 9941–9964, doi:10.5194/acp-12-9941-2012.

Loftus, A. M., and W. R. Cotton, 2014: Examination of CCN impacts on hail in a simulated supercell storm with triple-moment hail bulk microphysics. *Atmos. Res.*, **147–148**, 183–204, doi:10.1016/j.atmosres.2014.04.017.

——, ——, and G. G. Carrió, 2014: A triple-moment hail bulk microphysics scheme. Part I: Description and initial evaluation. *Atmos. Res.*, **149**, 35–57, doi:10.1016/j.atmosres.2014.05.013.

Maddox, R. A., 1976: An evaluation of tornado proximity wind and stability data. *Mon. Wea. Rev.*, **104**, 133–142, doi:10.1175/1520-0493(1976)104<0133:AEOTPW>2.0.CO;2.

Markowski, P. M., and Y. P. Richardson, 2010: *Mesoscale Meteorology in Midlatitudes*. 1st ed. Wiley-Blackwell, 407 pp.

——, C. Hannon, J. Frame, E. Lancaster, A. Pietrycha, R. Edwards, and R. L. Thompson, 2003: Characteristics of vertical wind profiles near supercells obtained from the Rapid Update Cycle. *Wea. Forecasting*, **18**, 1262–1272, doi:10.1175/1520-0434(2003)018<1262:COVWPN>2.0.CO;2.

Marwitz, J. D., 1972: The structure and motion of severe hailstorms. Part I: Supercell storms. *J. Appl. Meteor.*, **11**, 166–179, doi:10.1175/1520-0450(1972)011<0166:TSAMOS>2.0.CO;2.

Matson, R. J., and A. W. Huggins, 1980: The direct measurement of the sizes, shapes, and kinematics of falling hailstones. *J. Atmos. Sci.*, **37**, 1107–1125, doi:10.1175/1520-0469(1980)037<1107:TDMOTS>2.0.CO;2.

McCaul, E. W., and M. L. Weisman, 2001: The sensitivity of simulated supercell structure and intensity to variations in the shapes of environmental buoyancy and shear profiles. *Mon. Wea. Rev.*, **129**, 664–687, doi:10.1175/1520-0493(2001)129<0664:TSOSSS>2.0.CO;2.

Milbrandt, J. A., and M. K. Yau, 2005a: A multimoment bulk microphysics parameterization. Part I: Analysis of the role of the spectral shape parameter. *J. Atmos. Sci.*, **62**, 3051–3064, doi:10.1175/JAS3534.1.

——, and ——, 2005b: A multimoment bulk microphysics parameterization. Part II: A proposed three-moment closure and scheme description. *J. Atmos. Sci.*, **62**, 3065–3081, doi:10.1175/JAS3535.1.

——, and R. McTaggart-Cowan, 2010: Sedimentation-induced errors in bulk microphysics schemes. *J. Atmos. Sci.*, **67**, 3931–3948, doi:10.1175/2010JAS3541.1.

Miller, L. J., and J. C. Fankhauser, 1983: Radar echo structure, air motion and hail formation in a large stationary multicellular thunderstorm. *J. Atmos. Sci.*, **40**, 2399–2418, doi:10.1175/1520-0469(1983)040<2399:RESAMA>2.0.CO;2.

——, J. D. Tuttle, and C. A. Knight, 1988: Airflow and hail growth in a severe Northern Plains supercell. *J. Atmos. Sci.*, **45**, 736–762, doi:10.1175/1520-0469(1988)045<0736:AAHGIA>2.0.CO;2.

——, ——, and G. B. Foote, 1990: Precipitation production in a large Montana hailstorm: Airflow and particle growth trajectories. *J. Atmos. Sci.*, **47**, 1619–1646, doi:10.1175/1520-0469(1990)047<1619:PPIALM>2.0.CO;2.

Morrison, H., 2016a: Impacts of updraft size and dimensionality on the perturbation pressure and vertical velocity in cumulus convection: Part I: Simple, generalized analytic solutions. *J. Atmos. Sci.*, **73**, 1441–1454, doi:10.1175/JAS-D-15-0040.1.

——, 2016b: Impacts of updraft size and dimensionality on the perturbation pressure and vertical velocity in cumulus convection. Part II: Comparison of theoretical and numerical solutions and fully dynamical simulations. *J. Atmos. Sci.*, **73**, 1455–1480, doi:10.1175/JAS-D-15-0041.1.

——, and W. W. Grabowski, 2008: A novel approach for representing ice microphysics in models: Description and tests using a kinematic framework. *J. Atmos. Sci.*, **65**, 1528–1548, doi:10.1175/2007JAS2491.1.

——, J. A. Curry, and V. I. Khvorostyanov, 2005: A new double-moment microphysics parameterization for application in cloud and climate models. Part I: Description. *J. Atmos. Sci.*, **62**, 1665–1677, doi:10.1175/JAS3446.1.

——, G. Thompson, and V. Tatarskii, 2009: Impact of cloud microphysics on the development of trailing stratiform precipitation in a simulated squall line: Comparison of one- and two-moment schemes. *Mon. Wea. Rev.*, **137**, 991–1007, doi:10.1175/2008MWR2556.1.

Munich Re, 2013: Severe weather in North America: Perils, risks, and hazards. 2nd ed., 274 pp.

——, 2014: Overall picture of natural catastrophes in 2013 dominated by weather extremes in Europe and Supertyphoon Haiyan, 7 January 2014. [Available online at https://www.munichre.com/en/media-relations/publications/press-releases/2014/2014-01-07-press-release/index.html.]

Musil, D. J., A. J. Heymsfield, and P. L. Smith, 1986: Microphysical characteristics of a well-developed weak echo region in a high plains supercell thunderstorm. *J. Climate Appl. Meteor.*, **25**, 1037–1051, doi:10.1175/1520-0450(1986)025<1037:MCOAWD>2.0.CO;2.

NWS–San Antonio, 2016: April 12, 2016. Weather event summary. [Available online at http://www.weather.gov/media/ewx/wxevents/ewx-20160412.pdf.]

Nelson, S. P., 1983: The influence of storm flow structure on hail growth. *J. Atmos. Sci.*, **40**, 1965–1983, doi:10.1175/1520-0469(1983)040<1965:TIOSFS>2.0.CO;2.

——, 1987: The hybrid multicellular–supercellular storm—An efficient hail producer. Part II: General characteristics and implications for hail growth. *J. Atmos. Sci.*, **44**, 2060–2073, doi:10.1175/1520-0469(1987)044<2060:THMSEH>2.0.CO;2.

Parker, M. D., 2010: Relationship between system slope and updraft intensity in squall lines. *Mon. Wea. Rev.*, **138**, 3572–3578, doi:10.1175/2010MWR3441.1.

Picca, J. C., and A. V. Ryzhkov, 2012: A dual-wavelength polarimetric analysis of the 16 May 2010 Oklahoma City extreme hailstorm. *Mon. Wea. Rev.*, **140**, 1385–1403, doi:10.1175/MWR-D-11-00112.1.

Rasmussen, E. N., and D. O. Blanchard, 1998: A baseline climatology of sounding-derived supercell and tornado forecast parameters. *Wea. Forecasting*, **13**, 1148–1164, doi:10.1175/1520-0434(1998)013<1148:ABCOSD>2.0.CO;2.

——, and J. M. Straka, 1998: Variations in supercell morphology. Part I: Observations of the role of upper-level storm-relative flow. *Mon. Wea. Rev.*, **126**, 2406–2421, doi:10.1175/1520-0493(1998)126<2406:VISMPI>2.0.CO;2.

Rasmussen, R. M., and A. J. Heymsfield, 1987: Melting and shedding of graupel and hail. Part III: Investigation of the role of shed drops as hail embryos in the 1 August CCOPE severe storm. *J. Atmos. Sci.*, **44**, 2783–2803, doi:10.1175/1520-0469(1987)044<2783:MASOGA>2.0.CO;2.

Reisner, J., R. M. Rasmussen, and R. T. Bruintjes, 1998: Explicit forecasting of supercooled liquid water in winter storms using the MM5 forecast model. *Quart. J. Roy. Meteor. Soc.*, **124**, 1071–1107, doi:10.1002/qj.49712454804.

Rotunno, R., and J. B. Klemp, 1982: The influence of the shear-induced pressure gradient on thunderstorm motion. *Mon. Wea. Rev.*, **110**, 136–151, doi:10.1175/1520-0493(1982)110<0136:TIOTSI>2.0.CO;2.

——, and ——, 1985: On the rotation and propagation of simulated supercell thunderstorms. *J. Atmos. Sci.*, **42**, 271–292, doi:10.1175/1520-0469(1985)042<0271:OTRAPO>2.0.CO;2.

——, ——, and M. L. Weisman, 1988: A theory for strong, long-lived squall lines. *J. Atmos. Sci.*, **45**, 463–485, doi:10.1175/1520-0469(1988)045<0463:ATFSLL>2.0.CO;2.

Thompson, R. L., R. Edwards, J. A. Hart, K. L. Elmore, and P. Markowski, 2003: Close proximity soundings within supercell environments obtained from the Rapid Update Cycle. *Wea. Forecasting*, **18**, 1243–1261, doi:10.1175/1520-0434(2003)018<1243:CPSWSE>2.0.CO;2.

——, C. M. Mead, and R. Edwards, 2007: Effective storm-relative helicity and bulk shear in supercell thunderstorm environments. *Wea. Forecasting*, **22**, 102–115, doi:10.1175/WAF969.1.

van den Heever, S. C., and W. R. Cotton, 2004: The impact of hail size on simulated supercell storms. *J. Atmos. Sci.*, **61**, 1596–1609, doi:10.1175/1520-0469(2004)061<1596:TIOHSO>2.0.CO;2.

Wacker, U., and A. Seifert, 2001: Evolution of rain water profiles resulting from pure sedimentation: Spectral vs. parameterized description. *Atmos. Res.*, **58**, 19–39, doi:10.1016/S0169-8095(01)00081-3.

Weisman, M. L., and J. B. Klemp, 1982: The dependence of numerically simulated convective storms on vertical wind shear and buoyancy. *Mon. Wea. Rev.*, **110**, 504–520, doi:10.1175/1520-0493(1982)110<0504:TDONSC>2.0.CO;2.

——, and ——, 1984: The structure and classification of numerically simulated convective storms in directionally varying wind shears. *Mon. Wea. Rev.*, **112**, 2479–2498, doi:10.1175/1520-0493(1984)112<2479:TSACON>2.0.CO;2.

——, and R. Rotunno, 2000: The use of vertical wind shear versus helicity in interpreting supercell dynamics. *J. Atmos. Sci.*, **57**, 1452–1472, doi:10.1175/1520-0469(2000)057<1452:TUOVWS>2.0.CO;2.

Ziegler, C. L., P. S. Ray, and N. C. Knight, 1983: Hail growth in an Oklahoma multicell storm. *J. Atmos. Sci.*, **40**, 1768–1791, doi:10.1175/1520-0469(1983)040<1768:HGIAOM>2.0.CO;2.